STRUCTURE AND EVOLUTION OF AN OCEANIC MEGAMULLION ON THE MID-ATLANTIC RIDGE AT 27°N

By

Amy R. McKnight

B. A. , Geology
Colgate University, 1997

Submitted in partial fulfillment of the requirements of the degree of

Master of Science

at the

MASSACHUSETTS INSTITUTE OF TECHNOLOGY

and the

WOODS HOLE OCEANOGRAPHIC INSTITUTION

February 2001

Abstract

Megamullions in slow-spreading oceanic crust are characterized by smooth "turtle-back" morphology and are interpreted to be rotated footwalls of long-lived detachment faults. Megamullions have been analyzed in preliminary studies, but many questions remain about structural and tectonic details of their formation, in particular how the hanging wall develops in conjugate crust on the opposing side of the rift axis. This study compares the structure of an off-axis megamullion complex and its conjugate hanging wall crust on the Mid-Atlantic Ridge near 27°N. Two megamullion complexes, an older (M1) and younger (M2), formed successively on the west side of the rift axis in approximately the same location within one spreading segment. Megamullion M1 formed while the spreading segment had only one inside corner on the west flank, and megamullion M2 formed after the segment developed double inside corners west of the axis and double outside corners east of the axis. The older megamullion formed between ~22.3 and ~20.4 Ma, and the younger megamullion formed between ~20.6 and ~18.3 Ma; they are presently ~200-300 km off-axis.

Reconstruction poles of plate rotation were derived and plate reconstructions were made for periods prior to initiation of the megamullion complex (anomaly 6Ar, ~22.6 Ma), after the termination of megamullion M1 and during the development of megamullion M2 (anomaly 5E, ~19 9 Ma), and shortly following the termination of megamullion M2 (anomaly 5C, ~17.6 Ma). These reconstructions were used to compare morphological and geophysical features of both flanks at each stage of the megamullions' development. Megamullion M1's breakaway occurred at ~22.3 Ma and slip along this detachment fault continued and propagated northward at ~20.6 Ma to form the northern portion of M2. The exhumed footwall of megamullion M1 has weak spreading-parallel lineations interpreted as mullion structures on its surface, and it forms an elevated plateau between the enclosing segment boundaries (non-transform discontinuities). There was an expansion southward of the detachment fault forming megamullion M2 at ~20.1 Ma. It either cut a new detachment fault through megamullion M1, stranding a piece of megamullion M1 on the conjugate side (east flank), or it linked into the active detachment fault that was forming megamullion M1 or propagated into its hanging wall. The expanded detachment of megamullion M2 and the termination of megamullion M1 occurred during a time when the enclosing spreading segment roughly doubled in length and formed two inside corners. Megamullion M2 developed prominent, high-amplitude (~600 m) mullion structures that parallel the spreading direction for more than 20 km at each inside corner. Its detachment fault was abandoned ~ 18.6 Ma in the south and ~18.3 Ma in the north.

The gravity of this area demonstrates a consistent pattern of higher gravity corresponding to inside corners with thinner crust, apparently caused by fault exhumation of deep lithosphere, and lower gravity values corresponding to outside corners, indicating thicker crust, most likely a result of volcanic accretion. The gravity pattern of the area also helps with interpreting evolution of the megamullion complex. The southern section of megamullion M1 exhibits a series of inside-corner highs and elevated gravity values

while the northern section has lower gravity values until megamullion M2 began to form. This change coincides with the change of the northern segment edge from an outside corner to an inside corner. During the formation of megamullion M2, a gravity high developed over the center of the megamullion. After the termination of megamullion M2, the gravity values of both the northern and southern sections of the spreading segment decrease. This pattern suggests exhumation of higher-density lithosphere during formation of M1 and M2, and a return to more normal ridge-axis conditions following termination of the megamullion complex. The gravity of conjugate crust is consistently more negative, slightly decreasing in value during the formation of megamullion M2. This suggests that crust on the east flank is significantly thicker than that on the west flank, and that rift-axis magmatism may have slightly increased at the time that megamullion M2 formed.

We modeled gravity of an idealized structural cross-section of megamullion M2 to investigate possible structure and composition of the megamullion. Models with different detachment-fault angles and degrees of serpentinization of exhumed mantle that may be present in the megamullion were compared to Residual Mantle Bouguer Anomaly (RMBA) profiles. All models show gravity peaks slightly skewed towards the termination because higher-density rock is exposed closer to the termination than to the breakaway. Four models that varied the detachment fault angle show small variations that are unresolvable in the actual gravity data. Thus, the gravity profile of a megamullion is not diagnostic of its detachment fault angle from 30°to 60°/90°. Models that varied the degree of serpentinization of a lithospheric wedge beneath the megamullion show that slight variations in density give rise to large changes in the modeled gravity profiles. Comparison of model results against gravity profiles taken across megamullion M2 indicate that the magnitude of the gravity high associated with the megamullion is best explained by densities between 2800 kg/m^3 and 3000 kg/m^3 in the main body of the megamullion. This corresponds to peridotite serpentinized approximately 50%, or to gabbro (~2800 kg/m^3).

Table of Contents

2 Background

3 Methods

4 Reconstruction Results

5 Interpretations

1 Introduction

Detachment faults frequently develop on a sub-regional to regional scale in continental extensional environments; they are characterized by apparently normal, low-angle slip and displacement of tens of kilometers (Davis and Lister, 1988). It is common for the footwalls of detachment faults to expose middle to lower crustal metamorphic rocks (metamorphic core complexes). These rocks are believed to have undergone ductile deformation at depths greater than 10-15 km in the crust before undergoing brittle deformation during exhumation (Hodges et al., 1987). In comparison, the hanging wall may be thinned, but it consists of predominantly unaltered, unmetamorphosed rocks.

A similar kind of extension has been proposed to occur along mid-ocean ridges during periods of limited magma supply (Tucholke and Lin, 1994; Tucholke et al., 1996, 1997b; Cann et al., 1997). Bathymetric and sidescan-sonar images have revealed that areas with limited or intermittent magma supply sometimes exhibit domed massifs (megamullions) with corrugated surfaces (mullions). These domes span several kilometers to 20-30 km in diameter, are frequently up to 1. 5 km in relief, and have a surface interpreted to be the relict slip plane of a detachment fault. Many megamullions have been identified along the Mid-Atlantic Ridge, in the Australian-Antarctic Discordance, and on the Southwest Indian Ridge (Tucholke et al. 1996, 1998a; Cann et al., 1997; Casey et al., 1998; Dick et al., 1998; Fujioka et al., 1998). Additionally, there are incipient or poorly developed megamullions associated with areas of limited magma supply which are thought to represent proto-megamullions; i. e. , megamullions that were unable to fully develop due to a lack of sustained slip along a single fault (Tucholke et al., 1998a).

Morphologically, the turtle-back footwalls of metamorphic core complexes are similar in relief and extent to oceanic megamullions (Wright et al., 1974; Armstrong, 1982; Stewart, 1983; Tucholke et al., 1998a). For example, continental metamorphic core complexes have similar wavelengths (several tens of kilometers) and amplitudes (a kilometer or greater) to oceanic megamullions (Wright et al., 1974; Stewart, 1983; Tucholke et al. 1998a). Therefore, megamullions are thought to represent an extreme case of asymmetric seafloor spreading, with domes containing lower crustal and upper mantle materials on the footwall side of a mid-ocean ridge axis and a volcanic hanging wall on the other side (Figure 1) (Tucholke et al., 1998a).

Individual megamullions have been studied previously, but this study is the first attempt to examine both a megamullion and its conjugate crust on the opposing side of the rift axis. Analysis of bathymetric, gravity, and sidescan-sonar data on both ridge flanks is essential to understanding rift-axis conditions immediately prior to the development of a megamullion, during its formation, and immediately following its termination. In this study, we first summarize what is known about megamullions. We then analyze the formation and evolution of a well developed megamullion and its conjugate through structural analysis based on multi-beam bathymetry and sidescan-sonar records, and geophysical analysis of Residual Mantle Bouguer Anomaly (RMBA) patterns. We also model the gravity signature of the megamullion based on a structural cross-section predicted from the detachment fault model, and we compare the results to observed gravity data to constrain the structure and density of the megamullion.

2 Background

2.1 Segmentation along Mid-Ocean Ridges

Fundamental segmentation of the lithosphere is achieved by first-order (transform faults) and second-order (non-transform) ridge-axis discontinuities (Macdonald, 1986). Along slow-spreading ridges, discontinuities are associated with thinned or missing crust, and the crust in the corner between the active discontinuity and the spreading axis (inside corner) commonly exhibits irregular fault patterns with few volcanic features (Shaw, 1992; Shaw and Lin, 1993, 1996; Tucholke and Lin, 1994). Conversely, crust across the rift-axis along the inactive trace of the discontinuity (outside corner) has regular fault patterns, normal crustal thickness, and a regular distribution of volcanic features (Tucholke and Lin, 1994).

The accretion of magma along a slow-spreading ridge commonly appears to be focused at segment centers along the spreading axis (Whitehead et al., 1984: Crane, 1985; Lin et al., 1990). Compared to segment centers, segment ends at non-transform discontinuities along the Mid-Atlantic Ridge between 27°50'N and 30°40'N show large positive gravity anomalies equivalent to ~50% reduction in crustal thickness; in some cases, this accounts for a crustal-thickness variation of more than 3 km between segment centers and segment ends (Lin et al., 1990). This observation argues that minor non-transform discontinuities are not merely surficial *en echelon* cracks resulting from external stresses, but rather they are fundamental geodynamic divisions, marking boundaries of magmatic segmentation beneath the ridge. Total variation in crustal thickness along a segment seems to be related to segment length; longer segments have consistently greater variations in Mantle Bouguer Anomaly (MBA) values (Lin et al., 1990).

Segment morphology is related to the gravity anomalies. Abyssal hills along inside corners, which form at the rift valley walls through growth of normal faults, are more widely spaced and have greater throw than those at segment centers (Shaw, 1992). These features frequently lie outside the approximate boundary of RMBA lows that are typically centered within a spreading segment (RMBA bullseyes), and they correlate with RMBA highs toward segment ends, suggesting that the amagmatic extension associated with the large faults contributes to crustal thinning at segment ends, or vice-versa (Shaw, 1992; Shaw and Lin, 1993).

Cross-rift structural asymmetry tends to be concentrated near first- and second-order discontinuities at segment ends. Inside and outside corners, both along the ridge axis and off-axis, exhibit differences in crustal composition, RMBA, and morphology. Relict inside corners, proceeding off-axis from the ridge along flow lines, consist of a series of inside-corner bathymetric highs (Dick et al., 1981; Karson and Dick, 1983; Karson, 1990). These highs commonly exhibit strongly positive RMBA of up to 25 mGal above values at segment centers (Tucholke and Lin, 1994) and expose plutonic rocks as well as mantle ultramafics (Dick et al., 1981; Tucholke and Lin, 1994). In contrast, outside corners are typically covered by basalts and have lower relief and greater depths than inside corners (Severinghaus and Macdonald, 1988; Tucholke and Lin, 1994). Additionally, gravity values of outside corners are typically 10-20 mGal less than gravity values of inside corners (Tucholke and Lin, 1994).

2.2 Cyclicity of Melt Input

Analysis of gravity data suggests cyclicity of melt input along slow-spreading ridges. RMBA variations of 20 mGal or more along flow lines near segment centers have a periodicity of ~2-3 m. y. and imply crustal-thickness changes of at least 2 km (Tucholke and Lin, 1994; Pariso et al., 1995; Tucholke et al., 1997b, 1998a). It is likely that at this timescale, the variations are due to cycles of changing magmatism along the ridge axis. Gravity data also suggest that high-density material is not continuously emplaced at the inside corners; instead, peaks in gravity are sporadically distributed along the inside-corner trace outward from the ridge axis (Tucholke and Lin, 1994; Blackman et al , 1998). These gravity highs correlate with well developed inside-corner highs and megamullions, and they also are typically found where elevated RMBA (i.e. higher-density material) appears along-isochron over the remaining length of segments; this implies that they correlate with segment-wide reductions in magmatism and accompanying increases in tectonic extension.

Conditions during amagmatic and semi-magmatic periods may favor continued slip along existing faults rather than the creation of new faults. This would develop inside-corner highs composed of gabbro and peridotite as continued slip along the faults would exhume deeper crust. In contrast, increased magmatism would weaken the axial lithosphere and promote formation of new faults there, thus making continued slip along the older fault unlikely; the inward jumping of new fractures would create small-throw faults and small abyssal hills of basaltic composition. This process may explain the variable and intermittent development of inside-corner highs (Tucholke et al., 1998a).

2.3 Megamullions

Megamullions form at inside corners and are interpreted to be rotated footwalls of long-lived detachment faults (Figure 1). Corresponding outside corners are interpreted to be the hanging walls in which volcanic upper crust accretes. This crust is stripped from the inside-corner footwall and is carried to the ridge flank opposite the megamullion (Tucholke et al., 1998a).

Morphologically, megamullions exhibit consistent characteristics. Proceeding from where the feature initiated, the structure of a megamullion begins with an isochron-parallel ridge that defines where the detachment fault nucleated. This “breakaway” zone is typically an abyssal hill (ridge) whose younger side is interpreted to be the remnant fault plane. Following the breakaway there is an area of depressed crust that is typically several hundred meters deeper than the breakaway ridge. This zone rarely exhibits mullion structures although it frequently has isochron-parallel ridges up to hundreds of meters in relief (Tucholke et al., 1998a). These ridges may be formed by high-angle normal faults dissecting the detachment surface, or they may be klippen of the hanging wall stranded on the inside corner during slip on the detachment fault. Axis-ward from this depression, the dome of the megamullion rises as much as 1. 5 km. Its surface is corrugated by distinctive mullion structures with amplitudes ranging from below the lower limit of detection in conventional multi-beam bathymetry data (i.e., ~20 m) to 600 m (Tucholke et al., 1998a). These structures cap the surface of the exposure and are oriented parallel to flow lines and fault-slip direction. Long-distance continuity of mullions provide evidence that megamullions were formed by slip on single, long-lived faults. In one example next to the Atlantis Fracture Zone, 50–80% of the edifice exhibits mullion structures detectable with multi-beam bathymetry (Cann et al., 1997). The detachment surface off-axis may be dissected by high-angle normal faults that form in response to bending stresses during footwall rollover (Figure 1) (Manning and Bartley, 1994; Tucholke et al., 1998b). A megamullion is typically terminated in a valley-and-ridge structure parallel to the spreading ridge axis. It is thought that detachment faults are abandoned for one of two reasons: 1) a "ridge jump" forms a new fault nearer to the spreading axis, or 2) although rare, a rift propagates along axis to form a new fault (Tucholke et al., 1998a).

Dip angles of megamullion detachment faults within the lithosphere are uncertain. The fault surface on the older side of a megamullion dome often has cross-isochron dips between 0 to 10° away from the ridge axis. The fault dip at the termination averages 23° (plus or minus 8°) toward the ridge axis, which is likely a minimum value because of block rotation during transport from the rift valley to the ridge flank (Tucholke et al., 1998a). According to continental detachment fault models, the fault dip angle is expected to be ~30° or less (Thatcher and Hill, 1995). Some observations over megamullions appear to be consistent with this assertion; one study interpreted an intracrustal reflection from Cretaceous inside-corner crust to be a convex-upward detachment fault flattening updip from 30° to 20° within the basement and to less than 15° along the exhumed surface (Ranero et al., 1997). It was also shown that the interpreted heave of the fault was sufficient for normal extension to exhume lower crustal and upper mantle rocks (Ranero et al. 1997; Ranero and Reston, 1999).

There is significant evidence to suggest that megamullions expose cross-sections of the oceanic crust and have abnormally thin crust. Assuming 6-km-thick crust, a fault-dip angle of 60° would expose mantle at the surface only 6. 9 km from the breakaway, whereas the mantle would be exposed at the surface 8. 5 km and 12 km from the breakaway for dip angles of 45° and 30° respectively. All rock dredges and submersible sampling of the surfaces of currently identified megamullions have yielded serpentinized peridotites and gabbros (Auzende et al., 1994; Cannat et al., 1995; Cann et al., 1997; Casey et al., 1998; Tucholke et al., 1998a). In some cases, these rocks are exposed for flow line distances of as much as 35 km (Dick et al., unpub). The exposures need not be purely tectonic exhumation along faults in amagmatic rift environments. The presence of intrusives and extrusives interspersed with ultramafic rocks, as suggested by sampled gabbros (Tucholke and Lin, 1994; Dick et al., unpub.) and *in situ* volcanic cones on detachment surfaces (Tucholke et al., 1998b), indicate that intrusive magmatism and perhaps even seafloor volcanism may occur while detachment faulting exhumes deep-crustal and upper-mantle rocks.

Megamullions often have well developed magnetic anomalies, yet they are believed to consist of plutonic intrusives and upper mantle. However, recent research indicates that these observations are not mutually exclusive. In their magnetic survey of 0-29 Ma off-axis crust on the Mid-Atlantic Ridge, Tivey and Tucholke (1998) found that crustal magnetization is rapidly attenuated off-axis, indicating that magnetization in extrusive lava becomes only a background value off-axis. From this observation and analysis of ridge-flank magnetic patterns, they concluded that much of the off-axis magnetic signature is likely to be contained in plutonic crust.

The RMBA patterns over megamullions indicate crustal thickness variations, and they assist in interpreting megamullion evolution. Megamullions typically have an RMBA 20 to 25 mGal higher than normal crust found at segment centers, which suggests a reduction in crustal thickness of more than 2 km. If there is significant serpentinization, 2 km is likely a minimum reduction (Minshull, 1996). Gravity highs over most megamullions are not located near the terminations where it is thought that the deepest crust and mantle should be exhumed (Tucholke et al., 1998a). Rather, they are centered between the breakaway and termination or are shifted toward the breakaway. An exception is a megamullion near the Atlantis Fracture Zone in which the RMBA high is strongly skewed toward the termination (Blackman et al., 1998).

Two explanations of this gravity shift toward the breakaway have been proposed. One postulates that as the detachment fault continues to slip, there is increased seawater penetration into the fault zone which causes greater serpentinization of the mantle and results in a reduction of footwall density toward the termination (Tucholke et al., 1998a). The other asserts that the gravity reduction towards the termination is caused by increased magmatism at the ridge axis, possibly related to cyclic magmatism (Tucholke et al., 1998a). The latter is consistent with submersible observations at Dante's Domes megamullion on the Mid-Atlantic Ridge at 26.6° N where small volcanic cones appear on the flat detachment surface near the termination (Tucholke et al., 1998b).

2.4 Study Area

A detailed geological and geophysical study was conducted in 1992 on the western flank of the Mid-Atlantic Ridge between 25°25'N and 27°10' N, from the ridge axis out to 26–29 Ma crust (Tucholke et al., 1997b). In 1996, the eastern conjugate flank was surveyed out to 26 Ma crust (Tucholke et al., unpub. 1996). Each cruise collected Hawaii MR1 sidescan sonar, Hydrosweep multibeam bathymetry, gravity, and magnetics (Figures 2 and 3). This comprehensive data set is ideal for a geophysical investigation of megamullions and their conjugate crust.

The study area is located between the Kane Fracture Zone and the Atlantis Fracture Zone in a region of the Mid-Atlantic Ridge that has no major transform offsets along approximately 800 km of axis (Figure 2). Spreading centers instead are defined by a series of non-transform discontinuities (Sempere et al., 1993). As defined by bathymetry, sidescan-sonar records, and magnetic anomaly data, non-transform discontinuities delineate nine spreading segments in the study area (Figure 2). Some of these segments have been forming for more than 20 my.; all are subparallel to flow lines of relative plate motion and appear to have migrated independently of one another (Tucholke et al., 1997b; Tivey and Tucholke, 1998).

Within the study area there are at least six megamullions known (Tucholke et al, 1998a). A megamullion complex located on the western ridge flank between ~26°30' and 26°50' N and 46°45'W and 47°30' W, together with its east-flank conjugate, was chosen as the subject of the present study (Figures 4, 5). This complex is morphologically prominent and well developed, it has extensive survey coverage including the surrounding crust (Figures 2-5), and it exhibits well defined magnetic anomalies that allow accurate plate reconstruction of the crustal conjugates.

3 Methods

3.1 Geophysical Data

The study area has extensive multibeam bathymetry, sidescan sonar, gravity, and magnetics datasets. Ship tracks were oriented ~15-25° to plate flow lines in order to obtain significant sidescan-sonar backscatter from ridge-parallel structures while still obtaining potential-field data subparallel to flow lines (Tucholke et al., 1997b).

Hydrosweep multibeam bathymetry insonifies a seafloor swath equal to twice the water depth and it provided nearly 100% bathymetric coverage. The data were processed using "MB software" developed by Caress and Chayes (1996), with additional editing to reduce outer-beam edge effects. These data were then combined with GPS navigation data and gridded at 100 m to 500 m grid intervals.

HAWAII MR1 sidescan-sonar survey (north and south looking) was also performed on both ridge flanks. The sidescan-sonar system was towed ~100 m beneath the sea surface to acquire back-scatter imagery, and the data were processed and gridded assuming flat seafloor (Tucholke et al., 1997b).

The multibeam and sidescan-sonar datasets were used for structural interpretation of the megamullion and its conjugate (Figure 4a, 4b). Bathymetric maps (50 m contour interval) in conjunction with both north- and south-looking sidescan-sonar data were used to identify faults and to determine their sense and magnitude of offset. Both data sets were also used to identify and determine the extent of mullion structures. Megamullions are marked by an absence of ridge-parallel tectonic fabric and relatively little high-amplitude structure, unlike typical oceanic crust where sidescan-sonar records detect numerous ridge-parallel, inward-dipping faults. Flowline-parallel mullion structures are observable in both sidescan-sonar records and in shaded-relief bathymetric images where low-angle lighting accentuates the features (Figure 5).

The total magnetic field was measured in each survey using a towed proton-precession magnetometer. Both datasets were corrected for the regional field using the 1991 International Geomagnetic Reference Field (International Association of

Geomagnetism and Aeronomy, 1992) and merged with near-axis magnetics data from Purdy et al. (1990). The data were inverted for magnetization, but different processing parameters were used for data sets on the two ridge flanks. Both data sets had a similar range of long wavelengths filtered from their signal, but in processing the west-flank data a greater range of shorter wavelengths was filtered out than in the east-flank data (Tivey and Tucholke, 1998; Lin et al. unpub., 1997). This results in a more smoothed pattern of magnetic reversals in the west-flank data than in the east-flank data. This affects our ability to compare detailed magnetic patterns of the two flanks, but it does not affect our isochron interpretations. We used the magnetics data set only to identify isochrons to derive reconstruction poles and to determine sense of offset between spreading segments. Magnetic isochrons were identified on magnetization maps using the geomagnetic polarity timescale of Cande and Kent (1995). Both normal- and reverse-polarity isochrons were identified out to chron 8 on the eastern ridge flank and out to chron 13 on the western flank.

The gravity field of both ridge flanks was processed simultaneously to obtain free-air anomalies, and it was further reduced to obtain MBA values. This was done by subtracting from free-air values the attraction of the water/seafloor interface, plus the attraction of the crust/mantle interface assuming a uniform crustal thickness of 6 km; the assumed density of the water layer was 1030 kg/m^3, the crustal layer 2730 kg/m^3, and the mantle layer 3330 kg/m^3. RMBA values were then calculated by removing from the MBA values the effects of lithospheric cooling based on a thermal-age model (Phipps Morgan and Forsyth, 1988).

There is a marked difference between mean RMBA gravity values over the off-axis eastern and western ridge flanks in our study area (Figure 3). This contrast is regional and in some places is greater than 25 mGal, with east-flank values markedly less than west-flank values. This strong flank-to-flank asymmetry indicates that the origin of the difference cannot have been created on-axis. The more negative eastern values are likely due to the crust being at a higher temperature than the thermal-age model predicts, and/or thicker than normal. The most likely cause of such effects is hotspot influence, either from the Azores hotspot (~1900 km to the north-northeast) or the Great Meteor hotspot (~1300 km to the east-northeast).

Although the cause of the regionally reduced east-flank gravity is uncertain, we can determine the magnitude of the effect and remove it from our data to allow better comparisons of east- and west-flank gravity signatures. To do this, we determined the mean off-axis gravity value on each side (for all data points mapped in each reconstruction, as discussed later) and removed it from the data on that side, thus deriving values deviating from the mean. These data were plotted in the reconstructions discussed below. More detailed corrections were considered when we modeled gravity for reconstructed cross-sectional profiles. These are discussed in Section 5. 2. 3.

3.2 Derivation of Reconstruction Poles

To understand the evolution of the megamullion complex and its conjugate, we derived reconstruction poles for time periods prior to, during, and following megamullion formation (chrons 6Ar, 5E, 5C) and rotated geological and geophysical data accordingly to simulate ridge-axis conditions at those times. The relative past positions of adjacent lithospheric plates can be derived by matching positions of marine magnetic anomalies and fracture zones on either side of the ridge axis (Klitgord and Schouten, 1986). If both plates remain completely rigid, the rotation that restores these features to the ridge axis for a given geologic time also restores the plates to their relative position at that time (Figure 6). The latitude and longitude of the reconstruction pole, and the rotation angle about the pole, uniquely describe the plate reconstruction. Uncertainty in these three quantities depends on the extent of the magnetic lineation picks (the length of the plate boundary represented by the data), the inherent uncertainties in the picks, and the distance from the center of the data to the derived pole. Even reconstructions for plate boundaries with closely spaced, high-quality data will have different rotation-parameter uncertainties that vary with the geometric relationship between the data points and the pole position (Stock and Molnar, 1983).

We derived reconstruction poles for chrons 6Ar, 5E, and 5C. Using these poles, we were able to rotate geological and geophysical data to simulate ridge-axis conditions prior to the initial breakaway of the megamullion complex (at anomaly 6Ar), during its formation (anomaly 5E), and immediately after its termination (anomaly 5C). We used a least-squares technique developed by Hellinger (1981) and modified by Chang (1988) to derive reconstruction poles. This method uses correlative isochron points on each plate as model segments and estimates each segment as a segment of a great circle. In reality, model segments are not great circles, but each segment is short and the error in this approximation is negligible when compared to the errors in the data (Chang, 1988). Hellinger's method minimizes a least squares measure of fit as a function of the rotation parameters. The measure of fit represents a sum of squares of the weighted distances of fixed and a rotated data points for a given rotation (Hellinger, 1981). Chang (1988) modified this technique by using a spherical regression method to find concentrated error approximations.

The reconstructions made here for chrons 6Ar, 5E, and 5C are based on magnetic anomalies picked in spreading segments within our study area (Figures 2, 7, 8), within segments between the study area and the Atlantis Fracture Zone and the Kane Fracture Zone, and at both fracture zones so as to delineate the positions of these discontinuities. The points at which shiptracks cross the magnetic isochrons were picked as isochron data points (Figure 7); positions of these anomalies were assigned a 10-km error radius. Magnetic profiles published in the OMD atlas of the Mid-Atlantic Ridge between 22° and 38°N (Rabinowitz and Schouten, 1986) were also interpreted for selected spreading segments between Kane and Atlantis Fracture Zones; anomalies picked in these zones lengthened the plate boundary represented by the data and thus decreased the uncertainties in our reconstruction poles. Positions of these picks were assigned a 20-km error radius.

Additional points are needed to constrain rotations of anomaly picks to the correct conjugate segments. These are provided by fracture zone "pivot points," without which the Hellinger-Chang rotation may not necessarily rotate points to their conjugate segments, but rather to locations elsewhere along their great circles. Fracture-zone data points were chosen by a two-step process. Magnetic anomalies 6Ar, 5E, and 5C in segments to the north and south of Atlantis and Kane fracture zones were identified from the published OMD profiles. The trend of each segment's anomaly was then projected onto detailed bathymetric maps of the fracture zones, and the intersections with the interpreted traces of the fracture zones were chosen to represent the fracture-zone positions in the model (Figure 8).

Once the reconstruction poles for chrons 6Ar, 5E, and 5C were finalized (Figure 9), we rotated west-flank gridded geophysical data to their conjugates for each time period (Figures 8,10-18). Rotations were performed using a function based on C. Tapscott's Fortran library, translated by P. R. Shaw, and modified for MATLAB by C. Denham (pers. comm., 2000). The function performs a point-by-point rotation by calculating the rotation matrix for a rotation of "angle" degrees about the "ijk"th Cartesian axis. The rotated data were then combined with unrotated, conjugate data along the corresponding isochrons.

4 Reconstruction Results

4.1 Reconstruction Poles

Reconstruction poles derived here are given in Table 1 together with poles from Klitgord and Schouten (1986) for other anomalies close in time, and these are plotted in Figure 9. The error ellipses of our derived poles represent the upper and lower surfaces of the 95% confidence region. Inherent ranges of error result from uncertainties of the anomaly picks with respect to assigned errors, potential mis-assignment of picks to segments, and real "geologic noise" in magnetic-anomaly positions. The latter is particularly important at slow-spreading ridges, such as the present study, where variable crustal accretion and tectonism result in poorly developed and discontinuous magnetic anomalies (Vogt, 1986).

4.2 Reconstruction Discrepancies - Overlap and Underlap

Reconstructions based on derived poles for chrons 6Ar, 5E, and 5C regionally fit conjugate anomalies together well (Figures 8 a-c). However, at a finer scale (Figures 10,13,16) the fits are not perfect. Variations in fit between different segments are explained by the fact that different segments were in different tectonic and magmatic states at any given time; thus each segment may have recorded changes in the magnetic field differently. Consequently, no pole will perfectly align every segment with its conjugate at a given time. The derived poles represent a best fit along a much greater length of the ridge.

There are several mechanisms that could cause anomalous spacing of conjugate magnetic-anomaly pairs. Amagmatic (i.e., severe tectonic) extension may result in a partial recording of a magnetic signature, depending on the timing of a magmatic event relative to the tectonic extension. In this study, we identified isochrons at the peaks and troughs of the magnetization anomalies. Hence, if amagmatic extension truncated the recording of a magnetic-polarity interval, then the interpreted anomaly peak (or trough) would correlate to a time older than the actual anomaly peak (or trough) and underlap would occur in reconstructions. If magmatism occurred only late in the magnetic-polarity interval, the opposite would happen, and overlap could appear in reconstructions.

Underlap may also result from the difference between the time at which a plutonic rock (e.g., gabbro) is emplaced at a ridge axis and the time at which it cools through its Curie temperature (its magnetic-signature age), compared to the time at which rapidly cooling basalt acquires its magnetic-signature age. Cande and Kent (1976) asserted that magnetic-polarity boundaries should mimic crustal isotherms. Therefore, because basalt cools quickly, its polarity boundaries are near-vertical and are locked in at the spreading axis, and its emplacement age and magnetic-signature age are the same. However, gabbro cools more slowly, its isotherms are sloped, and its magnetic-signature age is younger than its emplacement age, i.e., it is locked in *off*-axis. Therefore, isochrons of segments that contain unusually large amounts of gabbro relative to basalt would be farther apart in reconstructions than isochrons of segments which contain "normal" basaltic and gabbroic sections of oceanic crust (Figure 19). Unusually large amounts of gabbro could occur at segment ends in areas of reduced magmatism, where extrusive magmatism does not occur. Or, the relative amount of gabbro could be enhanced where it is exhumed by faulting at inside corners.

Reconstructions at chrons 6Ar and 5E exhibit underlap between the conjugate flanks of segments F/G (Figures 10-15). This indicates that these magnetic-anomaly pairs are spaced farther apart than normal, possibly because magmatism occurred only in the early part of the time period represented, or because the segment has anomalously large amounts of gabbro compared to basalt. There is minor overlap between conjugate segments D/E in the reconstructions at chrons 5E and 5C (Figures 13-18), which may indicate magmatism only in the later part of the time period depicted.

4.3 Reconstructions

The bathymetric, magnetic, and gravity data of the western MAR flank were rotated to fit conjugate crust on the eastern flank in reconstructions at chrons 6Ar, 5E, and 5C (Figures 10-18). The bathymetric reconstructions do not incorporate the depression of the rift valley, which is 20 to 30 km wide and 1 to 3 km deep along the modern Mid-Atlantic Ridge in this region (Macdonald, 1986). The plate reconstructions show a good fit along the ridge between Kane Fracture Zone and Atlantis Fracture Zone (Figures 8a, 8b, 8c). There is also a good fit for segment E, south of the segment containing the megamullion complex (Figures 10-18). However, the reconstructions vary in quality of fit for segment G containing the megamullion complex, with reconstructions at chrons 6Ar and 5E showing up to ~10 km and up to ~20 km underlap, respectively.

Reconstruction of bathymetry at the time of chron 6Ar aligns the discontinuity between segments D and F well, and it indicates ~13 km of right-lateral offset along this discontinuity. The reconstructions (Figures 10-12) have underlap throughout segments D and F with the amount of underlap between segments D being less than the underlap between conjugate segments F. The discontinuity to the north of segment F is poorly defined at this time (Figure 10). An inside-corner high on the west flank in the southern part of segment F is just off-axis, rising ~900m. Another inside-corner high is located on the east flank in the northwest corner of segment D, with ~1. 5 km relief. Relatively normal abyssal hills with hundreds of meters of relief formed parallel to the ridge axis on either flank throughout both segments.

Bathymetric reconstruction at the time of chron 5E (Figure 13) shows good alignment of the discontinuity between segments D/E and F/G, but apparent mismatch of the discontinuity between segments G and H to the north. The reconstructions (Figures 13-15) exhibit greater underlap throughout segment G (~15 km) than in the reconstruction at chron 6Ar, but the fit in segment E is excellent. The southern discontinuity continues to exhibit right-lateral offset, expanding to ~30 km offset. This discontinuity is distinct and readily identifiable.

The discontinuity between segments G and H propagated northward on the west flank prior to chron 5E (white line, Figure 13), simultaneous with development of the northern breakaway of megamullion M2. At this time there is virtually no offset along the discontinuity (Figure 14). The northward propagation of the discontinuity is unclear on the east flank in this reconstruction. The likely location of the propagator (green line, Figure 13) is immediately west of the prominent and continuous abyssal hill at the western edge of the east-flank data in the reconstruction; this is at the eastern edge of the underlap in the reconstruction. This placement implies either 1) there was essentially no crust accreted on the east flank from the time of the northward propagation and until chron 5E, or 2) anomaly 5E was mis-identified on the east flank.

The chron 5C bathymetric reconstruction (Figure 16) aligns discontinuities to the north and south of segment G very well, and both flanks show bathymetric highs throughout the segment. The reconstructions (Figures 16-18) have an excellent fit with overlap or underlap less than ~2 km. Ridges on the eastern flank are abyssal hills oriented parallel to the ridge axis. On the western flank, two prominent elongate domes (mullion structures) oriented WNW-ESE formed on the megamullion. The southern discontinuity continues to have right-lateral offset (~16 km). The northern discontinuity has left-lateral offset (~11 km), representing a shift in sense-of-offset at the northern discontinuity between chron 6Ar and 5C. The opposite sense of the southern and northern offsets creates double-inside corners on the west flank (megamullion side) and double-outside corners along the conjugate east flank.

5 Interpretations

5.1 Structure of the megamullion complex (megamullions M1 and M2)

We identified megamullions based on their domal shape and the presence of mullion structures. The first of these features (M1) formed at approximately the same time that segment F split into segments G and H (Figure 20). The megamullion comprises essentially all of segment G and rises ~700 m above crust in the surrounding discontinuities. Sidescan-sonar images of the megamullion show no ridge-parallel fault structures that typically dominate images of "normal" crust. Instead, the images exhibit faint flow-line-parallel (WNW) structures, interpreted to be mullion structures. These mullion structures, also visible in shaded relief images of multibeam bathymetry (Figure 5), are 10 m to 200 m in amplitude and extend intermittently over the entire ~28 km length of the megamullion (Figure 20). RMBA gravity over megamullion M1 is ~18 mGal, roughly 10-14 mGal higher than in the adjacent discontinuities and 6 mGal higher than gravity over the older inside-corner high (Figure 18).

The east-flank conjugate of megamullion M1 exhibits high-relief abyssal hills and much deeper crust than the west-flank megamullion (Figures 16, 20). The gravity of the eastern conjugate is slightly elevated compared to older crust (Figure 18).

The second megamullion to form (M2) spans the entire length of a much-expanded segment G, forming during a time when the segment had inside corners on the west flank at both the northern and southern segment ends, and outside corners on the east flank (Figure 16). Sidescan-sonar images of this area are similar to those of megamullion M1; however, flow-line parallel fabric is more pronounced and indicates higher-amplitude mullion structures along the ~33 km length of megamullion M2. In particular, there are two prominent mullion structures, one each on the north and south portions of megamullion M2, that rise ~ 600 m and span from breakaway to termination. The gravity high associated with megamullion M2 is ~ 12 mGal higher than that of crust in surrounding discontinuities.

The crust conjugate to megamullion M2 is dominated by high-amplitude abyssal hills (Figure 16). The gravity values of the conjugate are slightly reduced compared to older crust (Figure 18).

Based on our reconstructions and structural mapping, we interpret development of the megamullion complex as follows (Table 2). Prior to ~22. 3 Ma (Figure 10), the southern boundary of segment F was a well defined, right-lateral-offset discontinuity, and segment F was just beginning to split into segments G and H; thus the northern discontinuity is poorly defined. At this time, the west flank had an inside corner just north of the southern discontinuity. An inside-corner high there had slightly elevated (~6 mGal) gravity values (Figure 12), but sidescan-sonar images and bathymetric data (Figures 5, 10) show no mullion structures over the feature. Therefore this inside-corner high appears not to be a megamullion.

The subsequent breakaway of megamullion M1 (Figure 13) is interpreted to occur at ~22. 3 Ma, a time when a northern segment boundary was developing and segment G was ~24 km in length. The northern discontinuity had right-lateral offset of about ~8 km. The southern discontinuity had right-lateral offset of ~13 km. The breakaway ridge was identified as such because it marks the youngest fault trace known to the west of the megamullion, and no mullion structures appear on older crust to the west of the ridge. The breakaway is followed on younger crust by a ~600 m depression and then by megamullion M1, both features being consistent with the megamullion model of formation (Figure 1). There is no development of normal abyssal hills over megamullion M1. From old to young crust across the breakaway, gravity becomes elevated (~12 mGal), peaking at the approximate midpoint of megamullion M1 (Figure 18). We interpret this as an indication of exhumation of higher-density material in the megamullion.

At ~20.6 Ma, during the period when megamullion M1 was being formed, the northern discontinuity propagated northward, increasing the segment length to ~50 km (Figure 13). There was virtually no offset between segments G and H at the time of this propagation. The discontinuity to the south continued to have a right-lateral offset of about ~20 km.

The northward propagator is the breakaway for megamullion M2. It is defined by a stairstep series of ridges followed by a depression to the east. Following the propagation, the detachment fault spanned the entire length of segment G. About the time of anomaly 5E (19.88 Ma), the northern discontinuity became a left-lateral offset (Tucholke et al., 1997). This created a double inside-corner setting for segment G on the west flank, and a double outside corner on the east flank. The gravity of the northern section of the segment prior to the formation of megamullion M2 was relatively low (Figure 18); however, following the breakaway of megamullion M2, the gravity increased ~6 mGal above previous values. We interpret this to mean that before the northern expansion of the discontinuity and breakaway of megamullion M2, the crust forming along this portion of the ridge was thicker and less dense than crust in megamullion M2. This is likely due to an exhumation of higher-density rocks in megamullion M2.

We interpret the termination of megamullion M1 to be marked by the eastern edge of the megamullion plateau in ~20.4 Ma crust (Figures 16, 20). If megamullion M1 terminated in the manner modeled in Figure 1, a termination ridge of stranded hanging wall should be evident on the western flank, gravity over the megamullion would be high while that over the termination ridge would be lower, and the gravity over the east-flank conjugate to the termination should be low. However, there is no identifiable termination ridge at which the mullion structures of megamullion M1 are truncated, and the gravity of the termination conjugate is elevated rather than reduced. This implies that the truncation of M1's detachment fault was located within megamullion M1. This could have stranded part of megamullion M1 on the eastern, conjugate flank, accounting for the observed rise in gravity there (Figure 18). The fault that cut into megamullion M1 and terminated slip on its detachment may have formed in response to magmatism along the southern portion of segment G. There is evidence from submersible dives along Dante's Domes megamullion that such magmatism may occur within the megamullion footwall (Tucholke et al., 1998b). Following termination of megamullion M1, there are no mullion structures observed, and gravity decreases (Figure 18); thus, the fault that truncated megamullion M1 was short-lived and magmatic extension (i.e., thicker crust) prevailed.

Shortly after megamullion M1's termination, however, another detachment fault must have formed, probably at ~20.1 Ma. Although there is no obvious breakaway ridge, the southern section of megamullion M2 was clearly developing, and a detachment fault apparently extended over the full length of the spreading segment, encompassing both inside corners and the segment center on the western ridge flank (Figure 16). Prominent mullion structures formed along both the northern and the southern portions of megamullion M2. The termination of the southern part of megamullion M2 is interpreted to occur at an isochron-parallel ridge at ~18. 6 Ma (Figure 16). Mullion structures can be traced up onto the west flank of this ridge. This ridge stairsteps northward into younger crust, reaching the northern tip of megamullion M2 at ~18. 3 Ma. We interpret megamullion M2 to have terminated according to the megamullion model (Figure 1), wherein an eastward "ridge jump" occurred from ~18.6 to ~18.3 Ma, isolating a piece of hanging wall on the megamullion side of the ridge; this now forms the isochron-parallel ridge at the termination. High gravity over megamullion M2 abruptly decreases across the termination (Figure 18), and this is interpreted to be caused by low density of the stranded hanging-wall ridge. Gravity of the conjugate remains low across the termination and then slightly decreases, suggesting that magmatism was constant to slightly increasing at the time of termination (Figure 18). Thus, it is possible, although not required, that the ridge jump and M2 termination were associated with increasing magmatism as suggested by the model in Figure 1.

5.2 Gravity Model

The generic detachment model for megamullion evolution (Figure 1) and our structural interpretations predict: 1) varying boundary configurations between lithologic units, depending on dip angle of the detachment fault, and 2) exhumation of a cross-section of ocean crust and upper mantle. To test whether these predictions can be constrained by gravity data, we modeled gravity across idealized geologic cross-sections of megamullion M2 and compared the results with observed gravity.

5.2.1 Model Procedure

We first created idealized crustal cross-section models that would result from fault dip angles of 60°, 45°, and 30° (Figure 21) and we then used a polygon method to model gravity that would result from these crustal models. Four polygons were used, representing the water layer, crustal layers on either side of the megamullion (two polygons), and mantle. Seafloor shape was based on three bathymetric profiles taken over megamullion M2. The average topography of these profiles was used as the water-crust interface. The distance between breakaway and termination was also identified in each profile, and the average distance was used as the distance between breakaway and termination in the idealized crustal model. The model was extended 450 km east and 450 west of the megamullion with assumed flat seafloor and constant water layer thickness (4. 4 km) to eliminate edge effects. The mantle polygon was assigned a maximum thickness of 40 km (sufficient to account for the effect of mantle on the gravity signature) and a density of 3330 kg/m^3. We used water density of 1030 kg/m^3, and crustal thickness of 6 km and crustal density of 2730 kg/m^3, consistent with J. Lin's processing of gravity data from shipboard processing (Section 3.1). Gravity across the model with varying structural configurations was calculated using code that measures the integrated vertical attraction of two- dimensional bodies having the specified polygon cross-sections (Blakely, 1995). Gravity values were calculated at nodes every 10 km along the cross-section.

The polygon code produces the equivalent of a free-air gravity profile for the specified structure. Both seafloor topography and subsurface interfaces influence this signal. To correct the model results to a mantle Bouguer anomaly, the attraction of the water-crust and crust-mantle interfaces (assuming constant 6-km-thick crust) were calculated and subtracted from the free-air anomaly. This is the same MBA correction made by J. Lin for the gravity survey data. Normally, residual mantle Bouguer anomaly would then be calculated by removing a thermal-age component from MBA. However, for the ~19-20 Ma crust in our study, the slope of isotherms that would be used in a thermal-age correction is negligible; therefore, we made no such correction, and lateral variation in our modeled MBA gravity is directly comparable to that in mapped RMBA gravity.

We tested different fault dip angles in the models because there has been a decades-long debate regarding the relative importance of high-angle verses low-angle faulting at metamorphic core complexes in continental extensional environments. Low-angle (≤30°) proponents argue that high pore-fluid pressures would make low-angle faulting favorable (Axen, 1992), and that displacement on low-angle normal faults is the only mechanism to accommodate large amounts of extension (Wernicke, 1981; Scott and Lister, 1992; Ruppel, 1995). Arguments for high-angle faulting (≥60°) focus mainly on Anderson's (1942) fault theory and the observed dip of fault planes in teleseismic earthquake data. Simple two-dimensional Mohr-Coulomb faulting theory suggests that the coefficient of internal friction is ~0. 6; therefore new faults should initiate at 30° to the direction of maximum compressive stress (σ_1). If σ_1 is assumed to be vertical for normal faulting, faults should initiate near dips of 60°. In oceanic crust, such dips are supported by fault-plane solutions of teleseismic events from the Mid-Atlantic Ridge and the Central Indian Ridge; these events have dips strongly concentrated around 45° and extending to 60° (Thatcher and Hill, 1991; 1995).

We included a model with a vertical interface at the termination of the megamullion (Figure 21). We did this because if a megamullion's detachment fault is abandoned because of renewed magmatism at the rift axis, the boundary between the megamullion rocks and melt intruding into fissures defining the termination could well be vertical.

We also used our gravity modeling to investigate possible constraints on composition of rocks within the megamullion. Although serpentinites are known to be present in at least some megamullions, the extent of serpentinites, peridotites, and gabbros is unknown. Thus, we varied densities in the model cross-section, simulating different rock compositions, to determine whether diagnostic effects appeared in the gravity signature. To accomplish this, a fifth polygon was added to the structural cross-section in the 45° fault model (Figure 22), and the gravity profile was calculated. In separate models, this fifth polygon's density was assigned values of 3330 kg/m^3, 3073 kg/m^3, 2815 kg/m^3, 2558 kg/m^3, and 2300 kg/m^3, representing 0%, 25%, 50%, 75%, and 100% serpentinization respectively (Klein and Hurlbut, 1993). The 2815 kg/m^3 density also approximates a gabbro composition, which normally falls in the range of 2700 to 2900 kg/m^3 (Klein and Hurlbut, 1993).

5.2.2 Gravity Model Results

In the structural model (Figure 21), a fault angle of 60° exhumes mantle at the seafloor only 6.9 km from the breakaway, whereas the mantle is exposed 8.5 km and 12 km from the breakaway for dip angles of 45°and 30° respectively. Despite these differences, gravity profiles for the 30°, 45°, 45°/vertical, and 60° fault models are generally similar to one another (Figure 23). They depart from the base gravity value (0) in approximately the same locations, peak at similar values in the same relative location, and have roughly equivalent slopes. The profiles show that regardless of fault-initiation angle, the gravity profile starts to increase ~20-30 km prior to the breakaway, it peaks more than halfway from the breakaway to the termination, and it returns to background levels ~30-40 km beyond the termination. These models assume no serpentinization, and the gravity anomaly over the megamullion is more than 100 mGal. There are two important implications of these model results. First, the gravity increase associated with exhumation of deep, dense rocks in a megamullion influences the gravity signature for more than a 50-km radius around the center of the megamullion. Second, the predicted gravity values are much too high compared to observed values (Figures 24-26). Thus, the megamullion cannot expose significant amounts of unaltered mantle peridotite at its center.

Although the differences between profiles for different fault-dip models are small, they are significant. Figure 27 shows how the 30°, 60°, and 45°/vertical profiles differ from the 45° model. Gravity near the breakaway in the 60° model profile increases toward younger crust at a steeper slope than in the other profiles (Figures 23, 27). In Figure 27, this is seen ~ 5 km following the breakaway, where the profile value is ~ 5 mGal higher than for a 45°/90° model and nearly 15 mGal higher than for a 30° fault. These differences directly reflect the distance at which model exposure of mantle occurs with respect to the breakaway.

The greatest difference between the profiles is in their skewness (Figures 23, 27). The peak of the 45°/vertical fault model is skewed slightly towards the breakaway, while the other models with decreasing fault angle (60° to 30°) are skewed progressively more toward the termination. This is clear in Figure 27, where approximately ~ 7 km following the termination, the 30° fault profile is ~20 mGal higher than the 45° fault profile, while the 60° and 45°/vertical fault models have profiles ~ 7 mGal and ~ 15 mGal lower, respectively. These differences directly reflect the subsurface distribution of high-density rocks in the model cross-section in the area of the termination.

Profiles calculated for different megamullion densities (e. g. , degrees of serpentinization) using the 45° fault model have a much greater variance in gravity values (Figure 28). Peak gravity values vary by up to 200 mGal between calculated profiles, demonstrating that a modest change in density results in a large change in profile values. These differences are large enough that they are easily resolvable in sea-surface gravity measurements. The implication of these results is that gravity profiles across megamullions can be diagnostic of the density contrast between the megamullion and its surrounding crust. The unserpentinized model has a density contrast of 600 kg/m^3; while density contrasts of 343 kg/m^3, 85 kg/m^3, -172 kg/m^3, and -430 kg/m^3 represent 25%, 50%, 75%, and 100% serpentinization respectively. The density contrast of gabbros is ~85 kg/m^3, equivalent to ~50% serpentinization in our model (Klein and Hurlbut, 1993).

5.2.3 Comparison of Gravity Models with Observed Gravity

To compare the gravity model results with observed gravity across the M2 megamullion, we considered three parallel gravity profiles (Figures 24-26, 29). These profiles are in the same locations as the three bathymetric profiles used for the structural model. They were selected because they are representative of the northern, central, and southern sections of the megamullion.

As was noted in section 3. 1 and as is clearly seen in Figure 29, gravity values on the east ridge flank are significantly lower than on the west flank. We attempted to adjust the eastern gravity values in order to eliminate this offset and to allow conjugate gravity values to be compared directly to one another and to our models. The procedure we used is based on the following argument. Although segment ends exhibit inside-corner to outside-corner asymmetry in crustal thickness and gravity values across the ridge axis (Tucholke and Lin, 1994), equal thicknesses of crust and equal gravity values should be generated on both ridge flanks adjacent to the segment center. Making this assumption, we determined gravity values at segment mid-points on both ridge flanks at a series of ages within the broad survey area, compared them, and used the differences to adjust the east-flank gravity values. We determined segment centers by first defining the limits of bounding discontinuities, then taking the midpoint (including its uncertainty) between these discontinuities. Gravity values were picked at these locations, with variation defined by the range of gravity values within the region of midpoint uncertainty.

Gravity differences (Δg) between the east- and west-flank picks were determined at the times of chrons 2A, 3, 3A, 4, 5A, 5AC/AD, 5Br, 5C, 5E, 6, 6Ar, 6BC, 6Ar, and 8. These differences are plotted in Figure 30 for each spreading segment considered. A best-fit line was determined for all Δg points with a reasonable error (± 4 mGal) in all segments (equation 2, Figure 30). Best-fits lines were also determined for other segments and segment groups. The data from segments F and G (on which megamullion M2 is located) appear to be atypical (equation 1; Figure 30); their difference plots far below the differences in other segments. These segments have two inside corners at ~20-15 Ma on the west side and two outside corners on the east side. Therefore, the assumption that crustal thickness and gravity are symmetrical across the axis at the segment center may not be valid. A best-fit was found to describe the Δg points of segments B, C, D, and E (equation 3; Figure 30), and an additional best-fit was determined for these segments in crust older than 17 Ma (the age of megamullions M1 and M2) (equation 4; Figure 30). The latter discounts the influence of large Δg variations in young crust, but it gives results that are nearly identical to equation 3 for the ages when the megamullions were formed.

Each of the four best-fit lines derived in Figure 30 was applied to the RMBA gravity profiles (A, B, C) of the eastern flank (Figures 24-26). However, none of these corrections provides a reasonable reconciliation of gravity levels between the east- and west-flank gravity profiles. Thus, we also made another kind of correction: we determined the gravity value at the location of megamullion termination in each profile (east and west), measured the Δg offset of these values for each of the three pairs of profiles, and calculated the average Δg. This offset was applied to the east-flank data (profile 5, Figures 24-26), and it provided a reasonable fit between gravity profiles over the two ridge flanks; hence, we used profiles corrected in this way for our interpretations.

Profiles of observed gravity over megamullion M2 were examined west of the megamullion's breakaway in an attempt to establish a gravity baseline (0 in the gravity model results) and thus to determine the relative magnitude of the gravity peak over the megamullion. However, a gravity base value cannot be established because this area has a complicated history of tectonic deformation and limited magmatism (Tucholke et al., 1997); thus, crust surrounding the megamullion may never have developed a "normal" baseline crustal section. Because a baseline gravity value cannot be established with certainty, the gravity profiles must be compared to the gravity model results restricted to the zone between breakaway and termination.

The three gravity profiles over megamullion M2 have generally similar shape (Figures 24-26). Gravity peaks midway between megamullion breakaway and termination is or skewed towards the breakaway, and the gravity values at the breakaways are greater than the values at smaller terminations. Profile A (Figure 24), the northernmost profile, has a narrow peak skewed towards the breakaway, followed to the east by another, lesser peak. Profile B (Figure 25), the central cross-section, has a single peak skewed slightly toward the breakaway. The southernmost profile, C (Figure 26), has a broad peak centered roughly between the breakaway and termination. The profiles show a 4-7 mGal increase in gravity over the megamullion compared to breakaway, and a decrease from peak to termination of approximately 10-13 mGal. The peak value, compared to the value at the breakaway, is consistent with megamullion density reflecting ~50% serpentinized peridotite and/or gabbro as predicted by the gravity model (Figure 28). The degree of serpentinization could be less if the crust surrounding the megamullion has densities higher than the 2730 kg/m^3 assumed in the gravity model. This is not unreasonable, given that this spreading segment has been significantly less magmatic than other segments in the study area (Tucholke et al., 1997).

Comparison of general trends in actual RMBA profiles and in the gravity model results indicates whether the model is a good representation of the geometry of the megamullion structure. Previous studies found that the gravity highs of megamullions tend to be located at the midpoint between breakaway and termination, or are skewed towards the breakaway (Tucholke et al., 1998a). Observation of the RMBA map (Figure 29) and the profiles (Figures 24-26) shows that the gravity high of megamullion M2 is generally centered between the breakaway and the termination or skewed toward the termination. This indicates that the geometry of the model is incorrect, and that megamullion M2 has a more complicated density structure than the structure that we modeled. Specifically, the position of the gravity peak (centered or skewed toward the breakaway) could be explained by increased serpentinization (decreased density) towards the megamullion termination. It also could be explained by an increase in extrusive or intrusive magmatism near the termination. Neither of these effects was considered in our gravity model.

While different fault angles predict large differences in modeled gravity values at megamullion termination (Figure 27), these differences are significantly reduced if density contrasts between the megamullion and surrounding crust are reduced by serpentinization or magmatism. The differences in modeled gravity values between breakaway and termination are also readily masked by such effects. We conclude that sea-surface gravity data do not provide an effective constraint on fault dip angles at megamullions.

6 Conclusions

We used bathymetry, sidescan-sonar, magnetics, and gravity data to interpret the structure and evolution of a megamullion complex and its conjugate crust located ~200-300 km off axis on the Mid-Atlantic Ridge in ~20 Ma crust. In plate reconstructions, we rotated these geophysical data sets to the times of anomaly 6Ar (~22.62 Ma), 5E (19.88 Ma), and 5C (17.58 Ma) to understand the evolution of the complex. The megamullion complex (M1 and M2) developed in the following sequence. Prior to ~22.3 Ma, a short (~24 km) spreading segment having a well defined discontinuity with right-lateral offset (~13 km) in the south and a poorly defined discontinuity in the north, developed an inside-corner high at the southern edge of the segment. At ~22.3 Ma a normal fault (detachment fault) broke through the entire segment. The northern discontinuity developed a well defined right-lateral offset (~8 km) and then was reduced to near-zero offset. At ~ 20.6 Ma the small-offset discontinuity propagated rapidly northward, lengthening the segment to about 50 km. This propagation also lengthened the detachment fault that had been forming megamullion M1 to the full length of the spreading segment, and slip on the northern extension of the fault initiated formation of megamullion M2. At ~20.4 Ma, slip on the megamullion M1 fault terminated, apparently because of increased magmatism at the southern end of the spreading segment. Subsequently, the detachment fault forming megamullion M2 expanded southward at ~20.1 Ma so that the fault again spanned the entire spreading segment. By chron 5E (~19.88 Ma) the discontinuity at the northern edge of the segment changed offset to left-lateral, thereby creating double inside corners at megamullion M2 on the west flank and double outside corners on the conjugate east flank. Major mullion structures up to ~600 m high formed along each of the inside corners on the west flank until development of the megamullion complex terminated between ~18. 6 Ma and ~18. 3 Ma. The termination may have been accomplished by a magmatic event, as suggested by a decrease in gravity (i.e., increase in crustal thickness) following the termination on the west flank. An increase in magmatism could weaken the rift-axis lithosphere and promote new faults to form inboard of the detachment, thus causing the abandonment of the detachment fault.

We modeled gravity signature across idealized cross-sections of megamullion M2 to determine the gravity profile created by specific structural and composition parameters. Our model results indicate 1) it is not possible to resolve fault-dip angle from gravity profiles over a megamullion, and 2) the gravity increases commonly observed in association with megamullions (~20-25 mGal) are best explained by ~50%

serpentinization of a 6-km thick wedge of peridotite (assuming mantle is exhumed), or by exhumation of gabbroic crust with comparable density of ~2800 kg/m^3.

7 References

Anderson, E. M., *The Dynamics of Faulting*, Oliver and Boyd, Edinburgh, 1942.

Armstrong, R.L., Cordilleran metamorphic core complexes - From Arizona to southern Canada, *Ann. Rev. Earth Planet. Sci.*, 10, 129-154, 1982.

Auzende, J.M., M.Cannat, P. Gente, J.P. Henriet, T. Juteau, J. Karson, Y. Lagabrielle, C. Mevel, and M. Tivey, Observations of sections of oceanic crust and mantle cropping out on the southern wall of Kane F.Z. (N. Atlantic), *Terra Nova*, 6, 143–148, 1994.

Axen, G.J., and J.M. Bartley, Field tests of rolling hinges: Existence, mechanical types, and implications for extensional tectonics, *J. Geophys. Res.*, 102, 20,515–20,537, 1992.

Blackman, D.K., J.R. Cann, B. Janssen, and D.K. Smith, Origin of extensional core complexes: Evidence from the Mid-Atlantic Ridge at Atlantis Fracture Zone, *J. Geophys. Res.*, 103, 21, 315-21, 333, 1998.

Buck, W.R., Flexural rotation of normal faults, *Tectonics*, 7, 959–973, 1988.

Cande, S.C., and D.V. Kent, Revised calibration of the geomagnetic polarity timescale for the late Cretaceous and Cenozoic, *J. Geophys. Res.*, 100, 6093-6095, 1995.

Cann, J.R., D.K. Blackman, D.K. Smith, E. McAllister, B. Janssen, S. Mello, E. Avgerinos, A.R. Pascoe, and J. Escartin, Corrugated slip surfaces formed at ridge-transform intersections on the Mid-Atlantic Ridge, *Nature*, 385, 329–332, 1997.

Cannat, M., C. Mevel, M. Maia, C. Deplus, C. Durand, P. Gente, P. Agrinier, A. Belarouchi, G. Dubuisson, E. Humler, and J. Reynolds, Thin crust, ultramafic exposures and rugged faulting patterns at the Mid-Atlantic Ridge (22°–24°N), *Geology*, 23, 49–52, 1995.

Caress, D.W., and D.N. Chayes, Improved processing of Hydrosweep DS multibeam data on the R/V Maurice Ewing, *Mar. Geophys. Res.*, 18, 631-650, 1996.

Casey, J.F., M.G. Braun, T. Fujiwara, T. Matsumoto, P.B. Kelemen and Scientific Party, Megamullions along the Mid-Atlantic Ridge between 14 and 16N: Results of Leg 1, JAMSTEC/WHOI Mode 98 survey (Abstract), *EOS Trans. AGU,* 79(45), F920, 1998.

Chang, T., Estimating the relative rotation of two tectonic plates from boundary crossing, *J. Am. Statist. Assoc.*, 83, 1178–1183, 1988.

Crane, K., The spacing of ridge-axis highs: Dependence upon diapiric processes in the underlying asthenosphere?, *Earth Planet. Sci. Lett.,* 72, 405-414, 1985.

Davis, G., and G.S. Lister, Detachment faulting in continental extension: Perspectives from the southwest U.S. Cordillera, *Spec. Pap. Geol. Soc. Am.*, 218, 133–159, 1988.

Dick, H.J.B., G. Thompson and W.B. Bryan, Low angle faulting and steady-state emplacement of plutonic rocks at ridge-transform intersections (Abstract), *EOS Trans. AGU*, 62(45), 406, 1981.

Dick, H.J.B., et al., Unpublished geological and geophysical survey of Atlantis Bank, Southwest Indian Ridge, 1998.

Hodges, K.V., J.D. Walker, and B.P. Wernicke, Footwall structural evolution of the Tucki Mountain detachment system, Death Valley region, southeastern California, *Geol. Soc. Spec. Publ.*, 28, 393-408, 1987.

Fujioka, K., C. Mevel, M. Cannat, K. Fujioka, T. Gamo, C.R. German, U. Muench, S. Ohta, L. M. Parson, R.C. Searle and Mode 98 Leg 3 Scientific Party, Preliminary results from the first submersible dives on the Southwest Indian Ridge (Abstract), *EOS Trans. AGU,* 79(45), 893, 1998.

Hellinger, S.J., The uncertainties of finite rotations in plate tectonics, *J. Geophys. Res.*, 86, 9312–9318, 1981.

International Association of Geomagnetism and Aeronomy (IAGA), Division V, Working Group 8, International geomagnetic reference field, 1995 revision, *Geophys. J. Int.*, 125, 318-321, 1992.

Karson, J.A., and H.J.B. Dick, Tectonics of ridge-transform intersections at the Kane Fracture Zone, *Mar. Geophys. Res.*, 6, 51-98, 1983.

Karson, J.A., Seafloor spreading on the Mid-Atlantic Ridge: Implications for the structure of ophiolites and oceanic lithosphere produced in slow-spreading environments, in *Proceedings of the Symposium TROODOS 1987*, edited by J. Malpas, E.M. Moores, A. Panayiotou and C. Xenophontos, Geologic Survey Departments, Nicosia, Cyprus, 547-555, 1990.

Klein, C., and C.S. Hurlbut, *Manual of Mineralogy*, John Wiley and Sons, Inc., New York, 1993.

Kleinrock, M.C., B.E. Tucholke, J. Lin, and M.A. Tivey, Fast rift propagation at a slow-spreading ridge, *Geology*, 25, 639-642, 1997.

Klitgord, K.D., and H. Schouten, Plate kinematics of the central Atlantic, in *Geology of North America*, vol. M, *The Western North Atlantic Region*, edited by P.R. Vogt and B.E. Tucholke, 351–378, Geol. Soc. of Am., Boulder, Co., 1986.

Lin, J., G.M. Purdy, H. Schouten, J.-C. Sempere, and C. Zervas, Evidence from gravity data for focused magmatic accretion of the Mid-Atlantic Ridge, *Nature*, 344, 627–632, 1990.

Macdonald, K.C., Mid-Ocean Ridges: Fine scale tectonic, volcanic, and hydrothermal processes within the plate boundary zone, *Ann. Rev. Earth Planet. Sci.*, 10, 155-190, 1982.

Macdonald, K.C., The crest of the Mid-Atlantic Ridge: Models for crustal generation processes and tectonics, in *The Geology of North America*, vol. M, *The Western North Atlantic Region*, edited by P.R. Vogt and B.E. Tucholke, pp. 51–68, Geol. Soc. of Am. Boulder, Colo., 1986.

Manning, A.H., and J.M. Bartley, Postmylonitic deformation in the Raft River metamorphic core complex, northwestern Utah: Evidence of a rolling hinge, *Tectonics*, 13, 596-612, 1994.

Minshull, T.A., Along-axis variations in oceanic crustal density and their contributions to gravity anomalies at slow-spreading ridges, *Geophys. Res. Lett.*, 23, 849–852, 1996.

Pariso, J. E. , J.-C. Sempere, and C. Rommevaux, Temporal and spatial variations in crustal accretion along the Mid-Atlantic Ridge (29°–31°30'N) over the last 10 m. y. : Implications from a three-dimensional gravity study, *J. Geophys. Res.*, 100, 17,781–17, 794, 1995.

Phipps Morgan, J., and D.W. Forsyth, Three-dimensional flow and temperature perturbations due to a transform offset: Effects on oceanic crustal and upper mantle structure, *J. Geophys. Res.*, 93, 2955-2966, 1988.

Purdy, G.M., J.-C. Sempere, H. Schouten, D.L. DuBois and R. Goldsmith, Bathymetry of the Mid-Atlantic Ridge 24°-31°N, *Mar. Geophys. Res.*, 12, 247-252, 1990.

Rabinowitz, P.D., and H. Schouten, Mid-Atlantic Ridge between 22° and 38°N, *Ocean Margin Drilling Program Regional Atlas Series*, Atlas 10, Marine Science International, Woods Hole, Ma, 1986.

Ranero, C.R., and T.J. Reston, Detachment faulting at ocean core complexes, *Geology*, 27, 983–986, 1999.

Ranero, C.R., E. Banda, and P. Buhl, The crustal structure of the Canary Basin: Accretion processes at slow spreading centers, *J. Geophys. Res.*, 102, 8075-8091, 1997.

Ruppel, C., Extensional processes in continental lithosphere, *J. Geophys. Res.*, 100, 24,187–24,215, 1995.

Scott, R.J., and G.S. Lister, Detachment faults: evidence for low-angle origin, *Geology*, 20, 833–836, 1992.

Sempere, J.-C., J. Lin, H.S. Brown, H. Schouten, and G.M. Purdy, Segmentation and morphotectonic variations along a slow-spreading center: The Mid-Atlantic Ridge (24°00'N-30°40'N), *Mar. Geophys. Res.*, 15, 153-200, 1993.

Severinghaus, J.P., and K.C. Macdonald, High inside corners at ridge-transform intersections, *Mar. Geophys. Res.*, 9, 253-367, 1988.

Shaw, P.R., Ridge segmentation, faulting and crustal thickness in the Atlantic Ocean, *Nature*, 358, 1992.

Shaw, P.R., and J. Lin, Causes and consequences of variations in faulting style at the Mid-Atlantic Ridge, *J. Geophys. Res.*, 98, 21,839-21,851, 1993.

Shaw, W.J., and J. Lin, Models of ocean ridge lithospheric deformation: Dependence on crustal thickness, spreading rate, and segmentation, *J. Geophys. Res.*, 101, 17,977–17, 993, 1996.

Stewart, J.H., Extensional tectonics in the Death Valley area, California: Transport of the Panamint Range structural block 80 km northwestward, *Geology*, 11, 153-157, 1983.

Stock, J.M., and P. Molnar, Some geometrical aspects of uncertainties in combined plate reconstructions, *Geology*, 11, 697-701, 1983.

Thatcher, W., and D.P. Hill, Fault orientations in extensional and conjugate strike-slip environments and their implications, *Geology*, 19, 1116-1120, 1991.

Thatcher, W., and D.P. Hill, A simple model for the fault-generated morphology of slow-spreading mid-oceanic ridges, *J. Geophys. Res.*, 100, 561–570, 1995.

Tivey, M.A., and B.E. Tucholke, Magnetization of 0 to 29 Ma crust on the Mid-Atlantic Ridge at 25°30' to 27°10'N, *J. Geophys. Res.*, 103,17,807–17,826, 1998.

Tucholke, B.E., and J. Lin, A geologic model for the structure of ridge segments in slow spreading ocean crust, *J. Geophys. Res.*, 99, 11,937–11,958, 1994.

Tucholke, B.E., J. Lin, and M.C. Kleinrock, Mullions, megamullions, and metamorphic core complexes on the Mid-Atlantic Ridge (Abstract), *EOS Trans. AGU*, 77(46), 724, 1996.

Tucholke, B.E., W.K. Stewart, and M. Kleinrock, Long-term denudation of ocean crust in the central North Atlantic Ocean, *Geology*, 25, 171–174, 1997a.

Tucholke, B.E., J. Lin, M.C. Kleinrock, MA. Tivey, T.B. Reed, J. Goff, G.E. Jaraslow, Segmentation and crustal structure of the western Mid-Atlantic Ridge flank, 25°25'-27°10' N and 0-29 m.y., *J. Geophys. Res.*, 102, 10203-10223, 1997b.

Tucholke, B.E., J. Lin, and M.C. Kleinrock, Megamullions and mullion structure defining oceanic metamorphic complexes on the Mid-Atlantic Ridge, *J. Geophys. Res.*, 103, 9857–9866, 1998a.

Tucholke, B.E., K. Fujioka, and T. Ishihara, Shinkai 6500 dives on Dante's Domes, a megamullion in the eastern rift mountains of the Mid-Atlantic Ridge at 26.6 degrees North (abstract), *EOS Trans. AGU*, 79(45), 45, 1998b.

Vogt, P.R., Magnetic anomalies and crustal magnetization, in *Geology of North America*, vol. M, *The Western North Atlantic Region*, edited by P.R. Vogt and B.E. Tucholke, 229-256, Geol. Soc. of Am., Boulder, Co, 1986.

Wernicke, B., Low-angle normal faults in the Basin and Range Province: Nappe tectonics in an extending orogen, *Nature*, 291, 645–648, 1981.

Whitehead, J.A., Jr., H.J.B. Dick, and H. Schouten, A mechanism for magmatic accretion under spreading centers, *Nature*, 312, 146–148, 1984.

Wright, L.A., J.K. Otton, and B.W. Troxel, Turtleback surfaces of Death Valley viewed as phenomena of extensional tectonics, *Geology*, 2, 53-54, 1974.

TABLE 1

Central Atlantic North American plate to African plate finite-difference poles of rotation: Reconstruction poles

Anomaly(Age)	Pole Latitude	Pole Longitude	Rotation Angle (N.A. to Af. Plate)	Source
13 (33.62 Ma)	76.41°N	7.12°E	9.81°	2
6Ar (22.62 Ma)	79.61°N	10.49°E	6.21°	1
6 (20.85 Ma)	79.57°N	37.84°E	5.29°	2
5E (19.88 Ma)	77.22°N	86.16°E	4.65°	1
5C (17.58 Ma)	76.79°N	89.76°E	4.08°	1
5 (10.5 Ma)	79.08°N	77.95°E	2.41°	2

Source 1 are poles derived in this study.
Source 2 are poles of Klitgord and Schouten (1986)

TABLE 2

Event	Approximate Age (Ma)
Breakaway of megamullion M1	22.3
Breakaway of northern portion of megamullion M2	20.6
Termination of megamullion M1	20.4
Breakaway of southern portion of megamullion M2	20.1
Termination of southern portion of megamullion M2	18.6
Termination of northern portion of megamullion M2	18.3

9 Acknowledgments

Acquisition of geological and geophysical data used in this study was supported by ONR grant N00014-90-J-1621 and by NSF grant OCE-9503561. My research was supported by a fellowship from Woods Hole Oceanographic Institution.

I am grateful to my advisor, Brian Tucholke, for making this thesis a success through his guidance and expertise. I would also like to thank Maurice Tivey and Charles Denham for their help at critical times with pesky computer programs. Jian Lin was a tremendous help throughout the research project, especially with the gravity modeling section. I greatly appreciate the patient training and advice given to me by Lori Dolby. I would also like to thank my thesis committee: Peter Clift, Maurice Tivey, and Susan Humphris for all of their efforts and advice. To the "DIAL room groupies" - Allegra, Jen, and Mark; without your timely advice there would have been many more late nights, and I thank you for your humor and insights. I would additionally like to thank Julia Westwater and Susan Humphris for insisting that I "keep the faith".

To my friends and family, this would not have been possible without your love and support. Amy, for over twenty years you have known when I needed to laugh, cry, and be kicked in the butt; I consider myself extremely blessed to have you as a friend. To the best officemate in the world, thank you for everything. Bryan, you constantly remind me of the importance of being happy; thank you for being you. Finally, to my parents, I cannot put into words how much your love and support has meant to me over the years. You gave me the courage to follow my dreams and make some tough decisions; I know that by following your example, I can never fail. I love you very much.

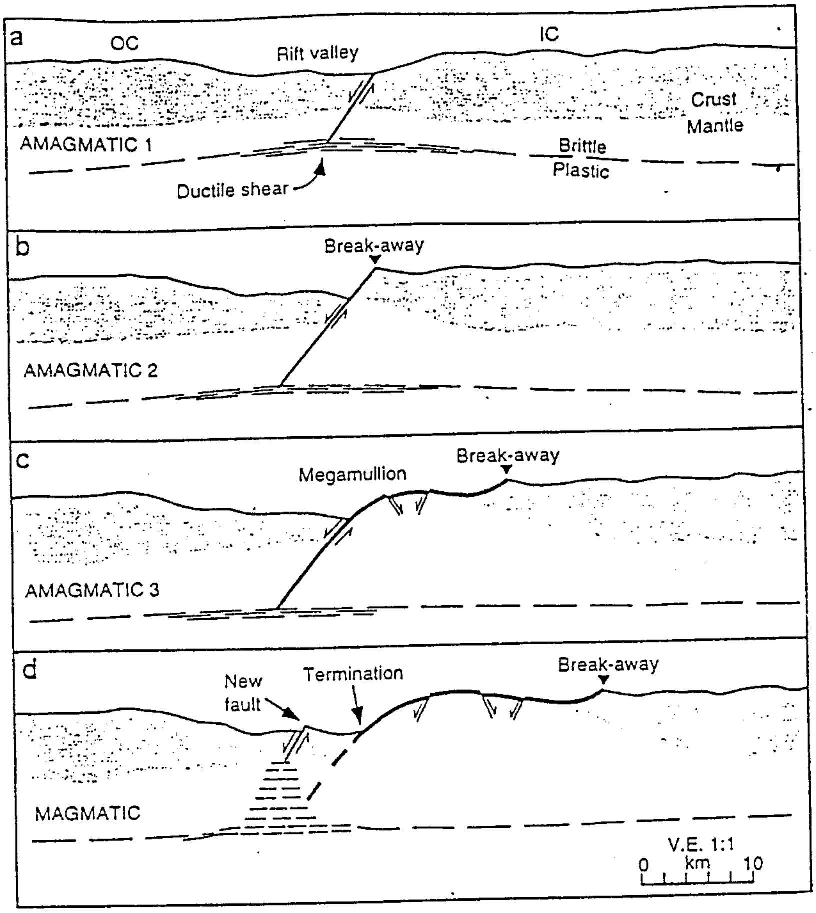

From Tucholke et al., 1998a

Figure 1: Idealized evolution of a megamullion, from Tucholke et al., 1998a. A) Detachment fault cuts through the brittle lithosphere during the beginning of a phase of spreading characterized by limited magma supply. B) The brittle/ductile transition zone deepens and the toe of the fault follows. C) Slip along the fault exposes lower-crustal and upper-mantle rocks. The doming of the footwall is created by footwall rollover (Buck, 1988). D) A magmatic phase in spreading begins, weakens the axial lithosphere, a new fault forms, and the detachment is abandoned.

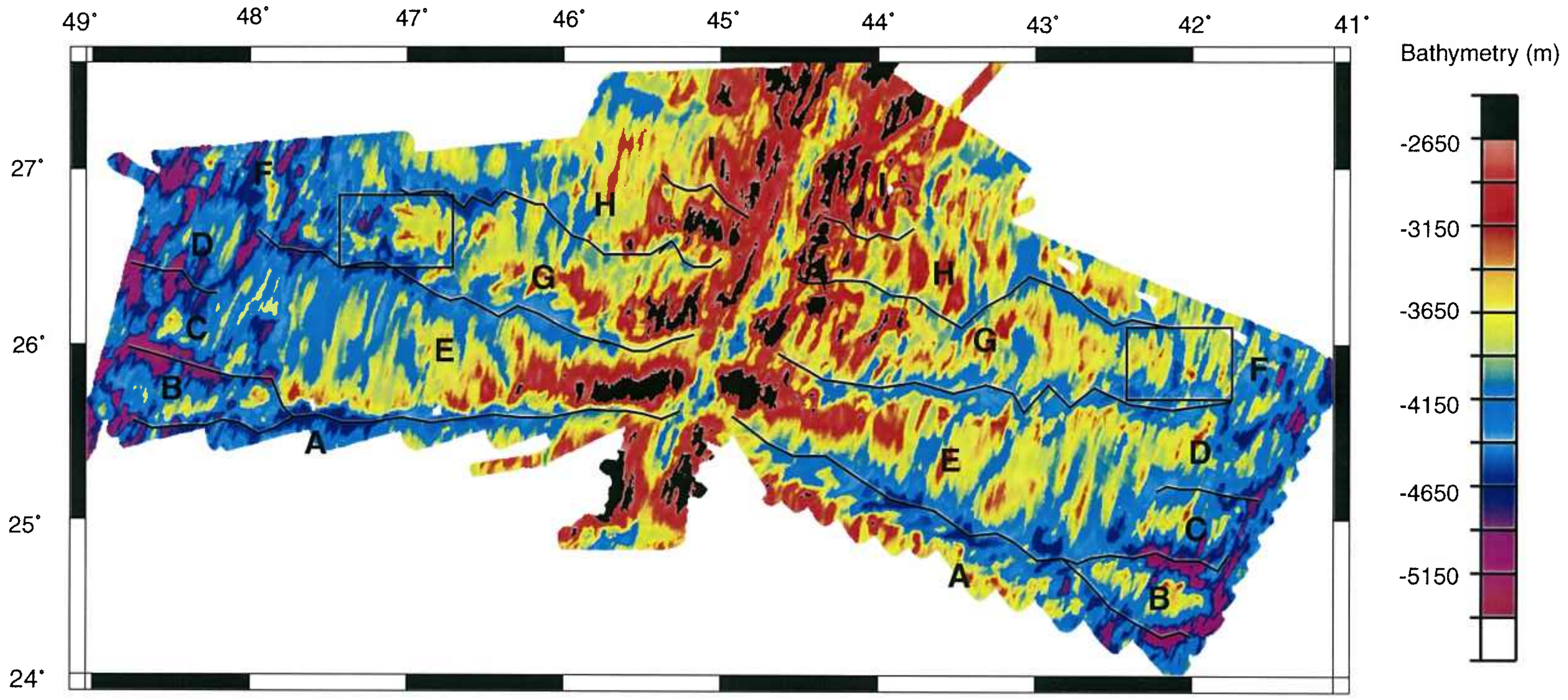

Figure 2: Bathymetry and simplified segmentation pattern of the study area out to chron 8 on the east flank and chron 13 on the west flank; nine spreading segments are defined and labeled from Tucholke et al. (1997). Discontinuities are indicated by solid black lines. The area of the megamullion complex studied here is boxed on the west flank, and its approximate conjugate is boxed on the east flank.

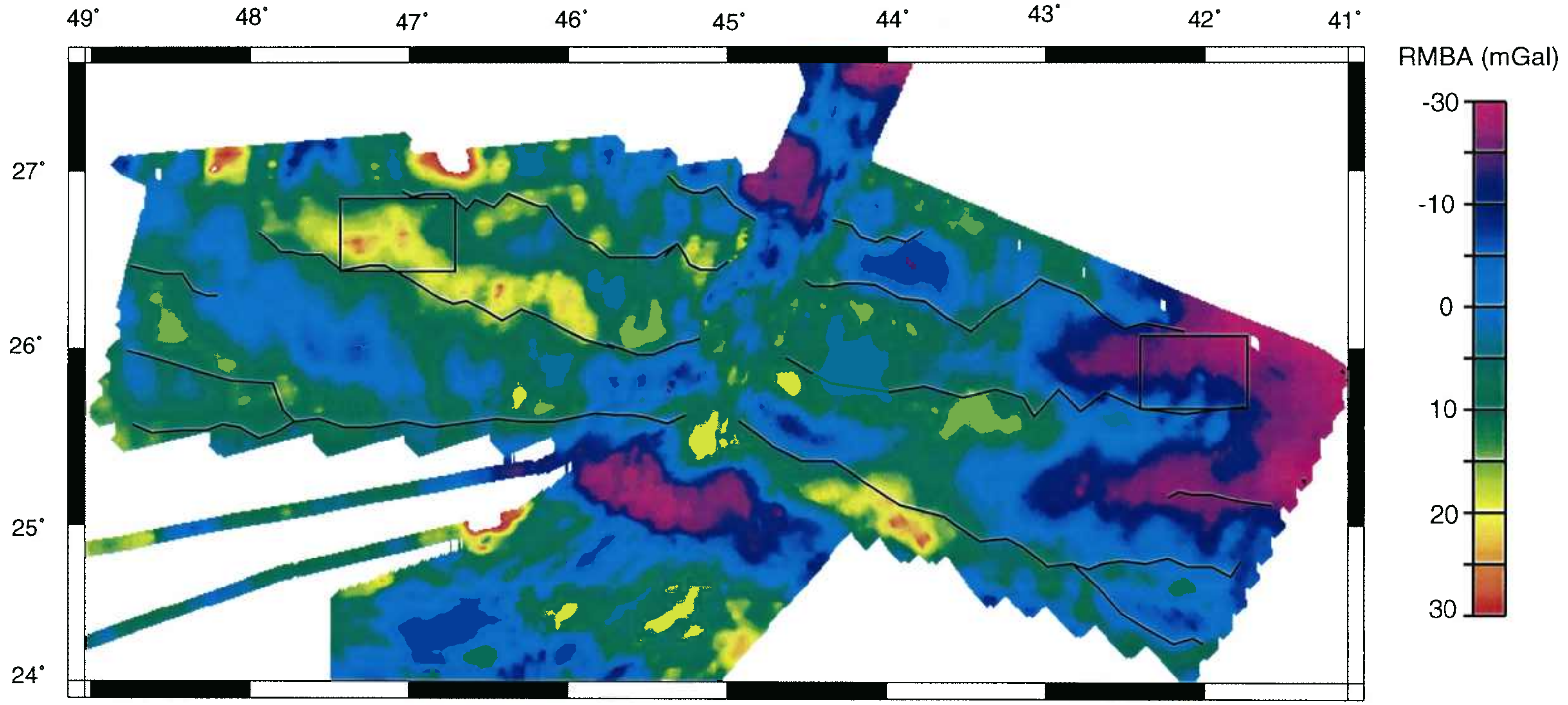

Figure 3: Residual mantle Bouguer gravity anomalies in the study area, with discontinuities delineated as black lines as in Figure 2. The area of the megamullion complex is boxed on the west flank, iand ts approximate conjugate is boxed on the east flank.

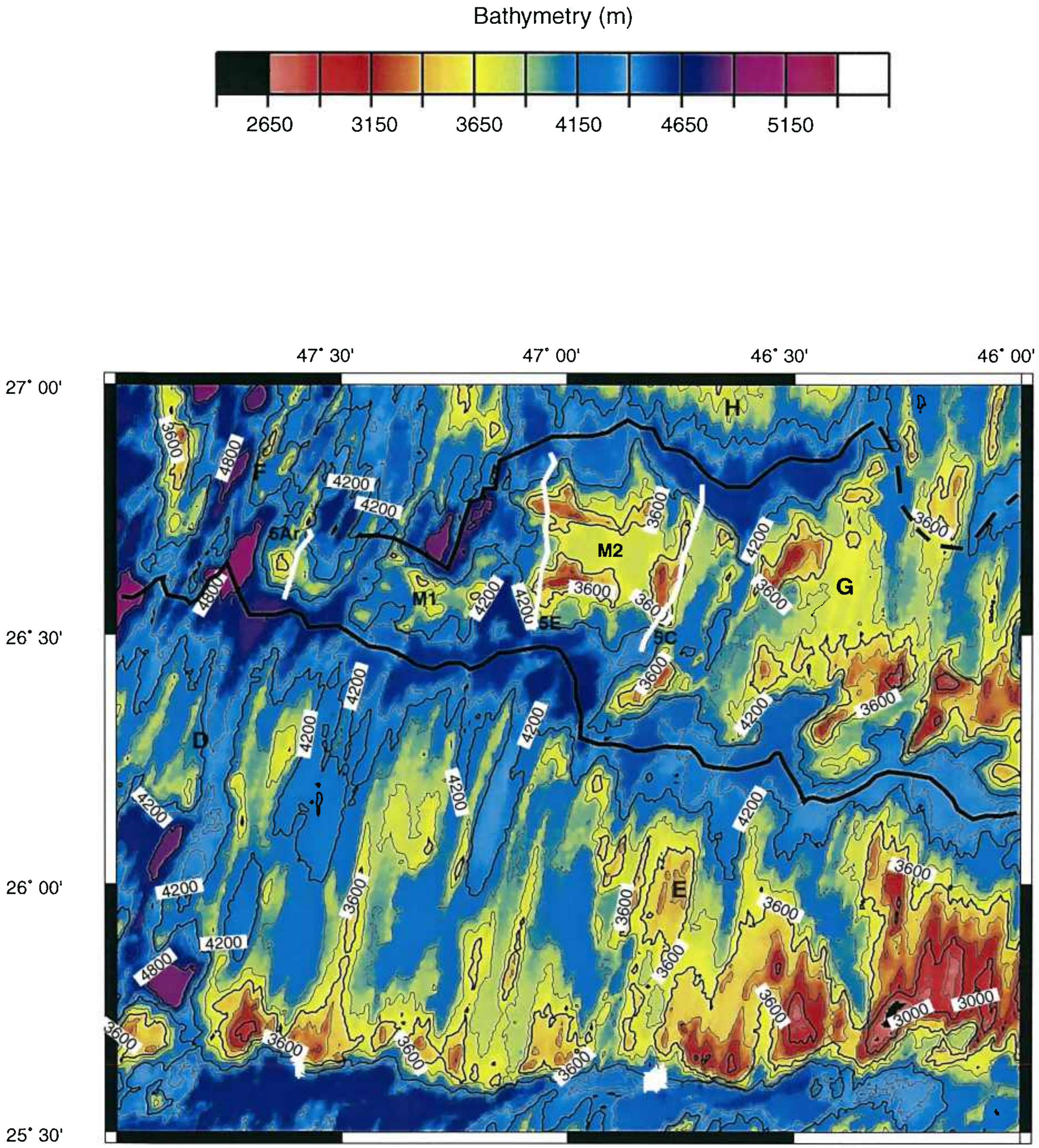

Figure 4a: Bathymetry of the megamullion complex studied here (M1 and M2) and its surrounding crust. M1 and M2 are the older and younger megamullions (respectively) in the complex. Discontinuities are shown by black lines. Magnetic anomalies 6Ar, 5E, and 5C are delineated in white.

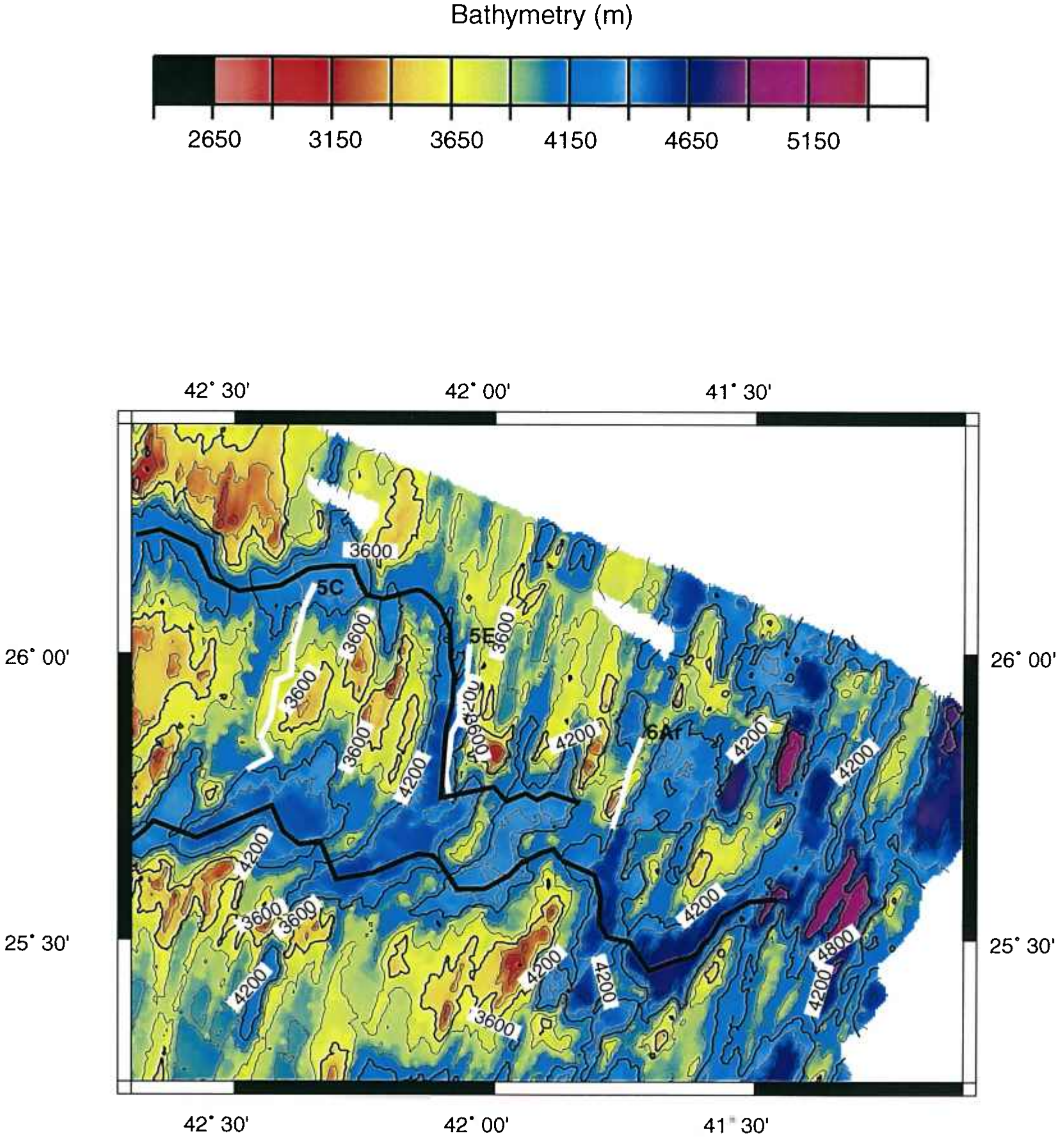

Figure 4b: Bathymetry of crust conjugate to the megamullion complex in Figure 4a. Discontinuities are delineated in black. Magnetic anomalies 6Ar, 5E, and 5C are shown in white.

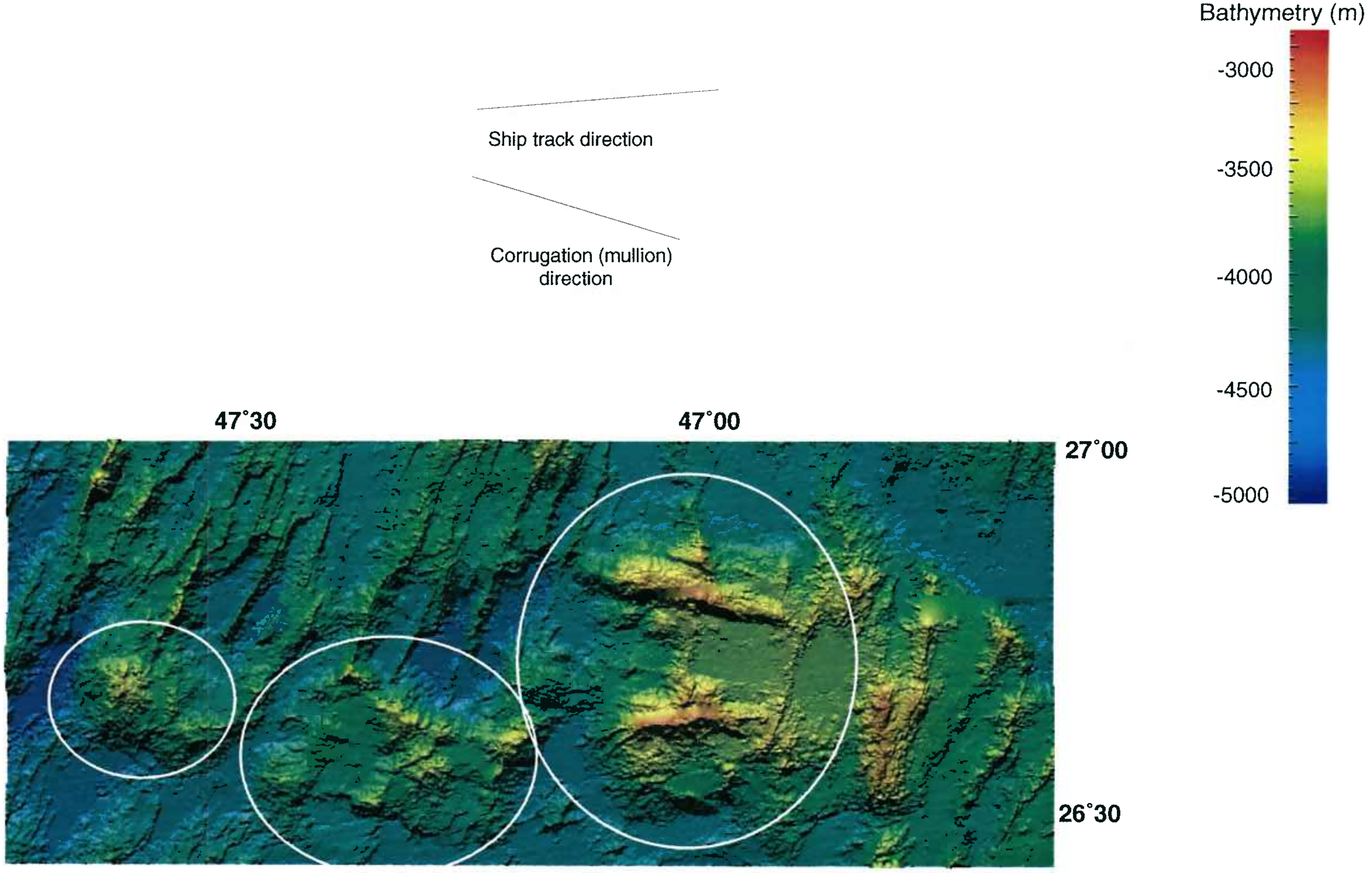

Figure 5: Shaded-relief (illuminated from NW) image of mulitbeam bathymetry of the megamullion complex studied on the west flank of the Mid-Atlantic Ridge and its surrounding crust. Areas circled in white are an old inside-corner high (left), the first-formed megamullion (M1,center), and the later-formed megamullion (M2, right). Mullion structures trending WNW are observable over the lengths of M1 and M2. The shiptrack direction is ~E-W, so it is clear that the lineations identified as mullions are not beam point artifacts. Segment boundaries are defined in Figure 4a.

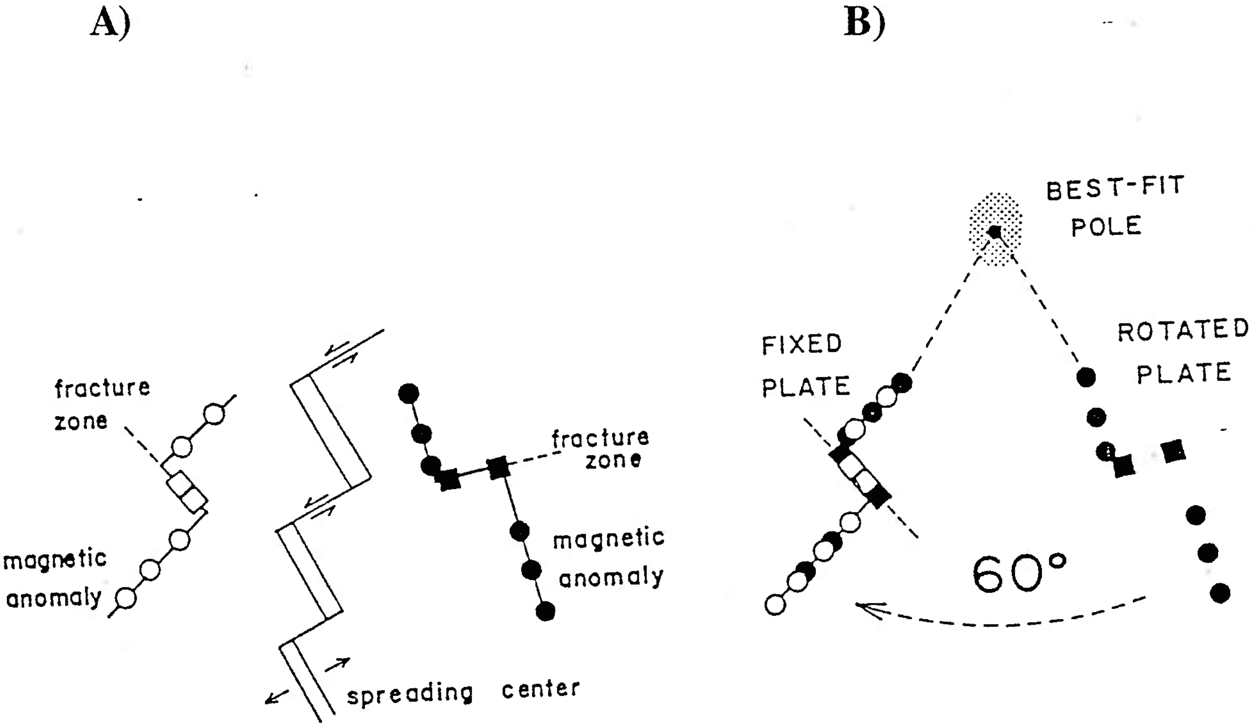

Figure 6: A) Idealized picks of magnetic anomalies for plate reconstruction; isochrons are represented by circles and fracture zones by squares. B) Rotated plate is rotated to fixed plate using best fit pole and rotation angle (from Stock and Molnar, 1983).

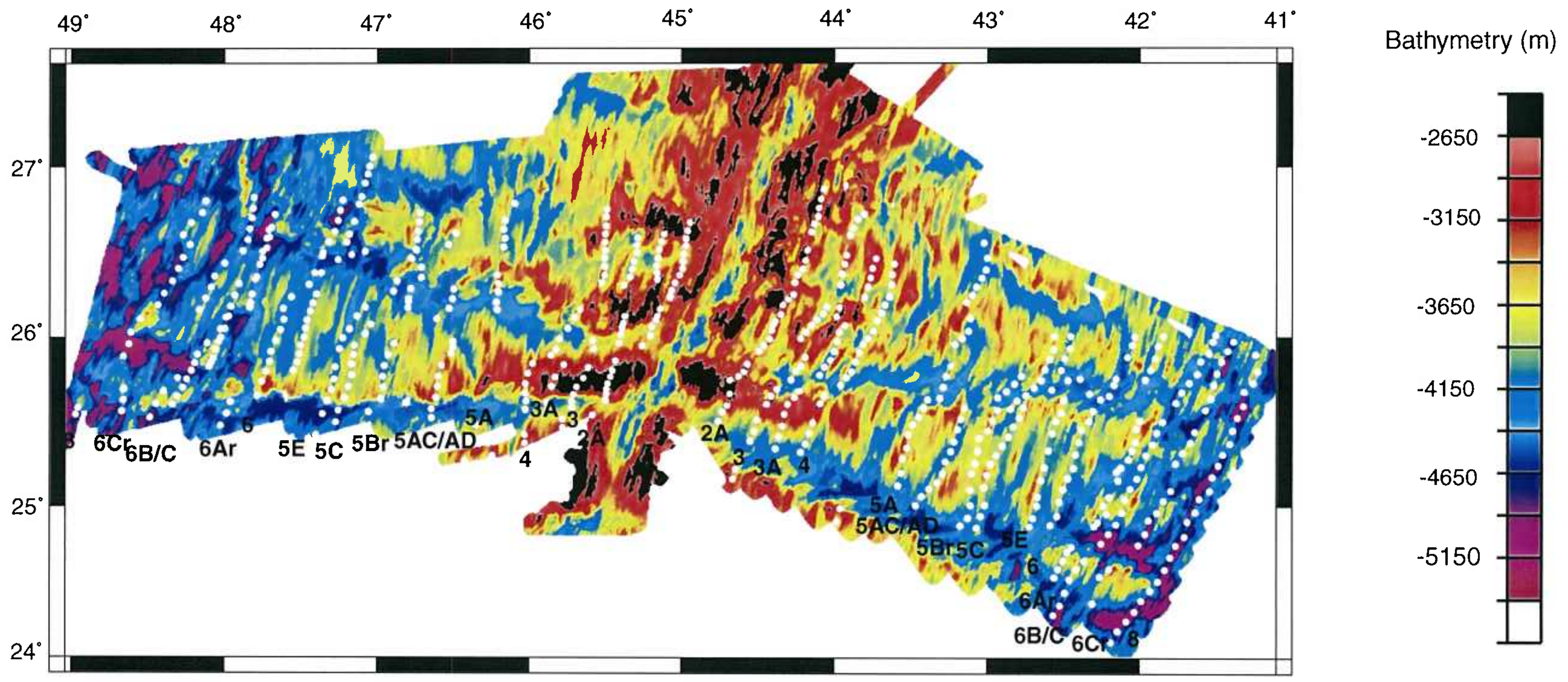

Figure 7: Bathymetry of study area with magnetic isochron interpretations of anomaly 2A, 3, 3A, 4, 5A, 5AC/AD, 5Br, 5C, 5E, 6, 6Ar, 6B/C, 6Cr, and 8. Each white point is a ship-track intersection with an interpreted isochron.

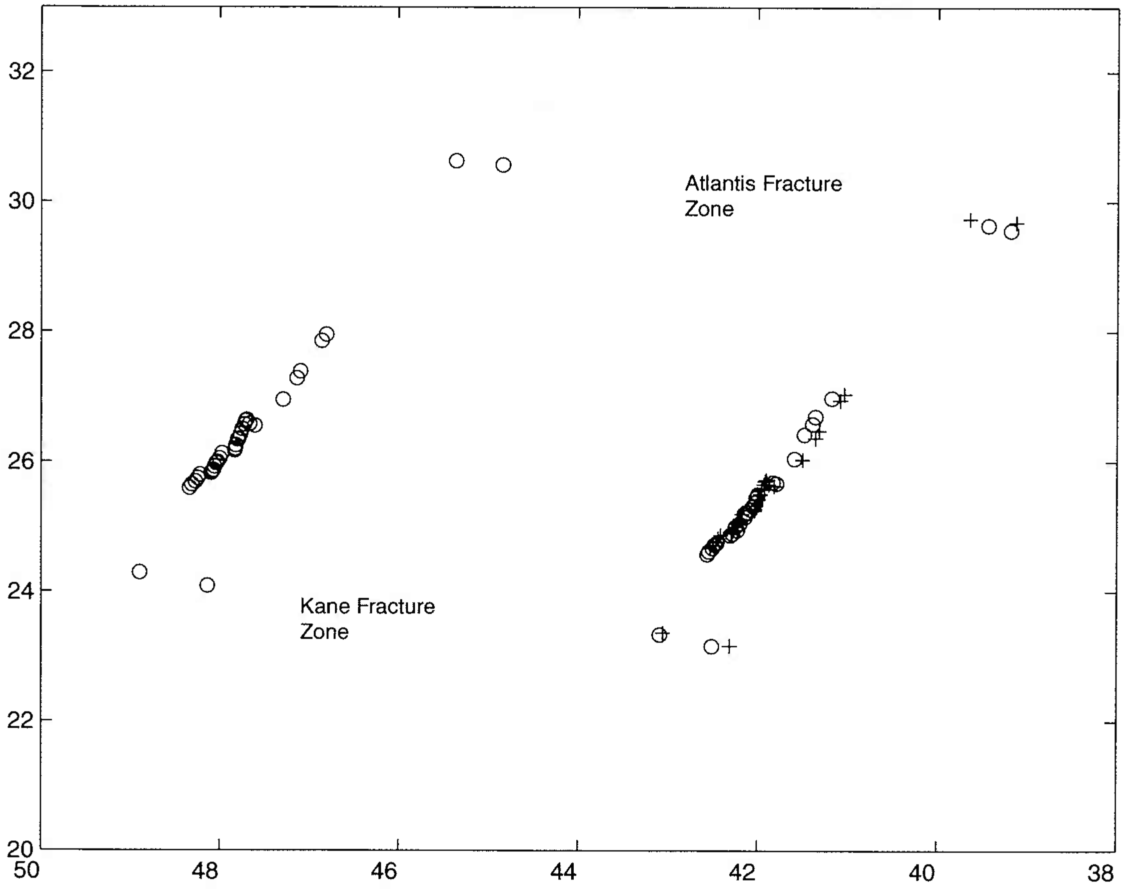

Figure 8a: Isochron picks for anomaly 6Ar on the east and west flanks of the Mid-Atlantic Ridge (circles) and west-flank picks (crosses) rotated according to the reconstruction pole (79.61˚N, 10.49˚E, 6.21˚) derived in this study. For scale, circles on picks are ~15 km in diameter.

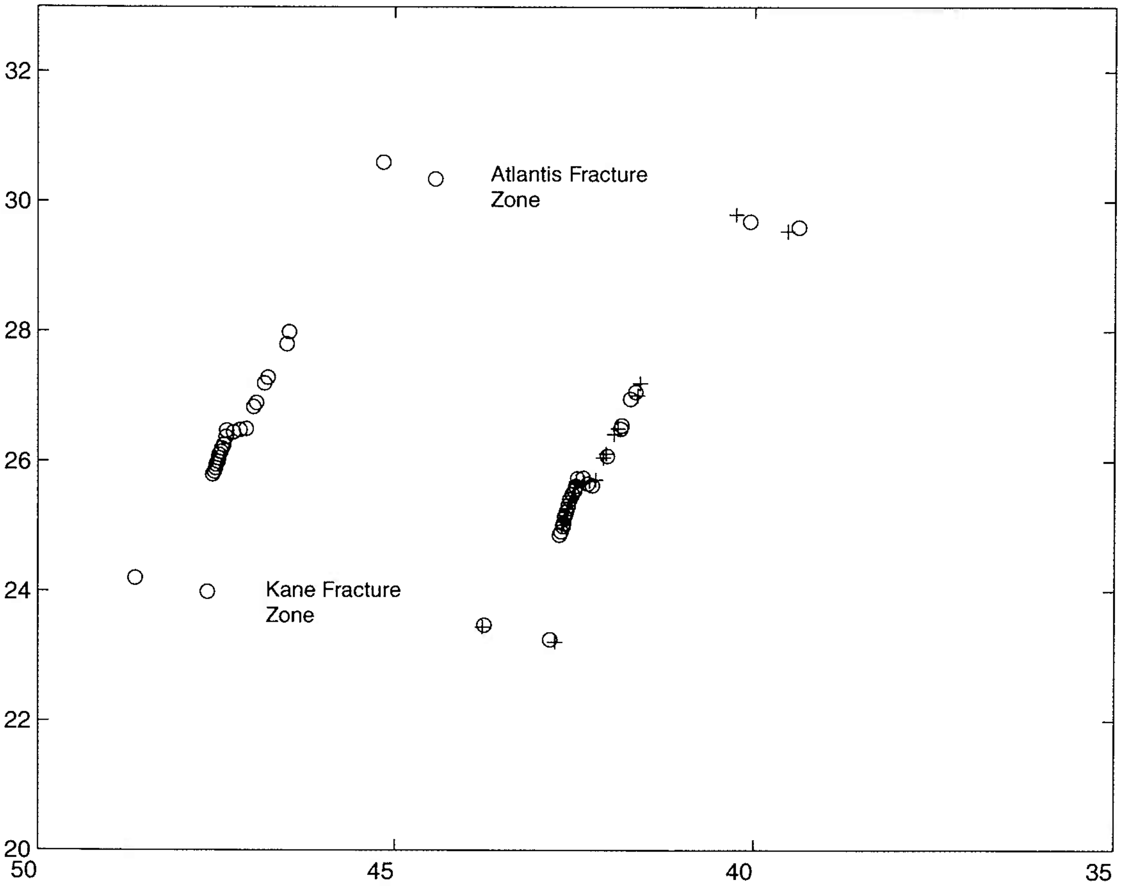

Figure 8b: Isochron picks for anomaly 5E on the east and west flanks of the Mid-Atlantic Ridge (circles) and the west-flank picks (crosses) rotated according to the reconstruction pole (77.22˚N, 86.16˚E, 4.65˚) derived in this study. For scale, circles on picks are ~15 km in diameter.

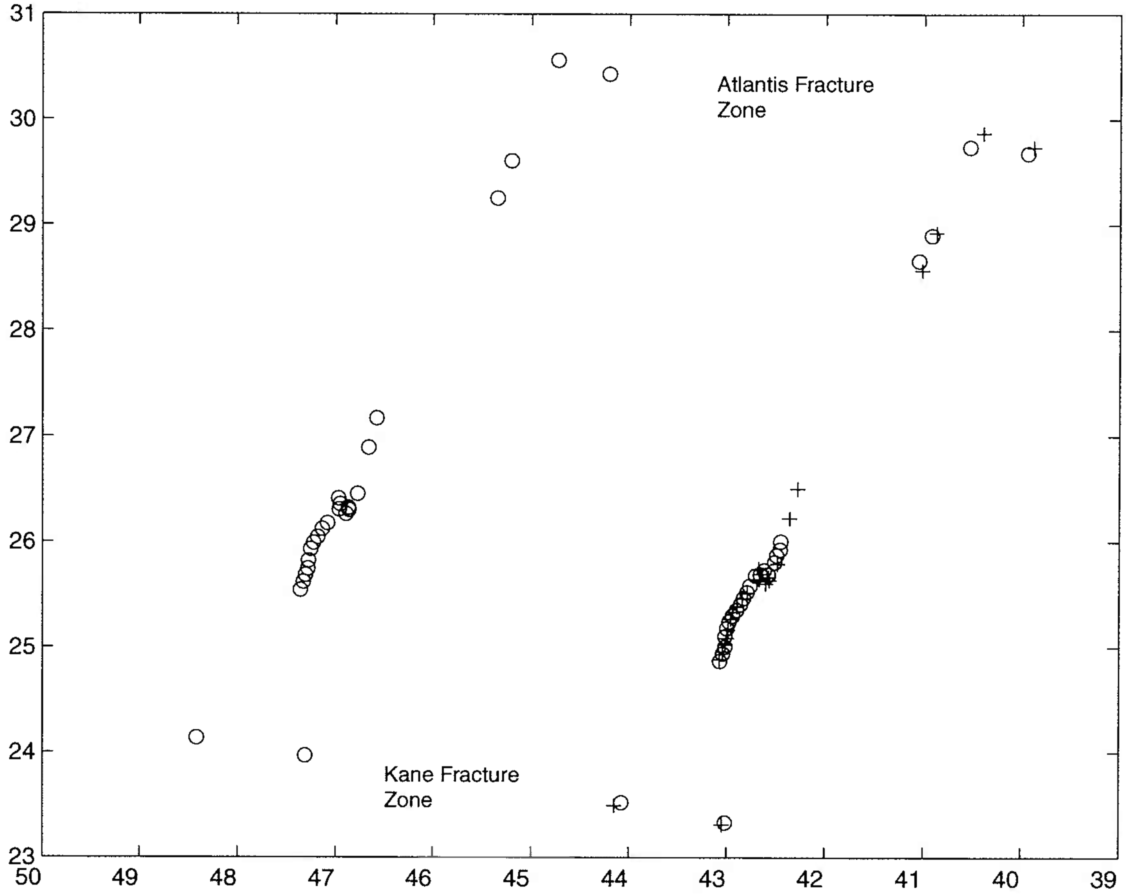

Figure 8c: Isochron picks for anomaly 5C on the east and west flanks of the Mid-Atlantic Ridge (circles) and west-flank picks (crosses) rotated according to the reconstruction pole (76.79°N, 89.76°E, 4.08°) derived in this study. For scale, the circles on picks are ~15 km in diameter.

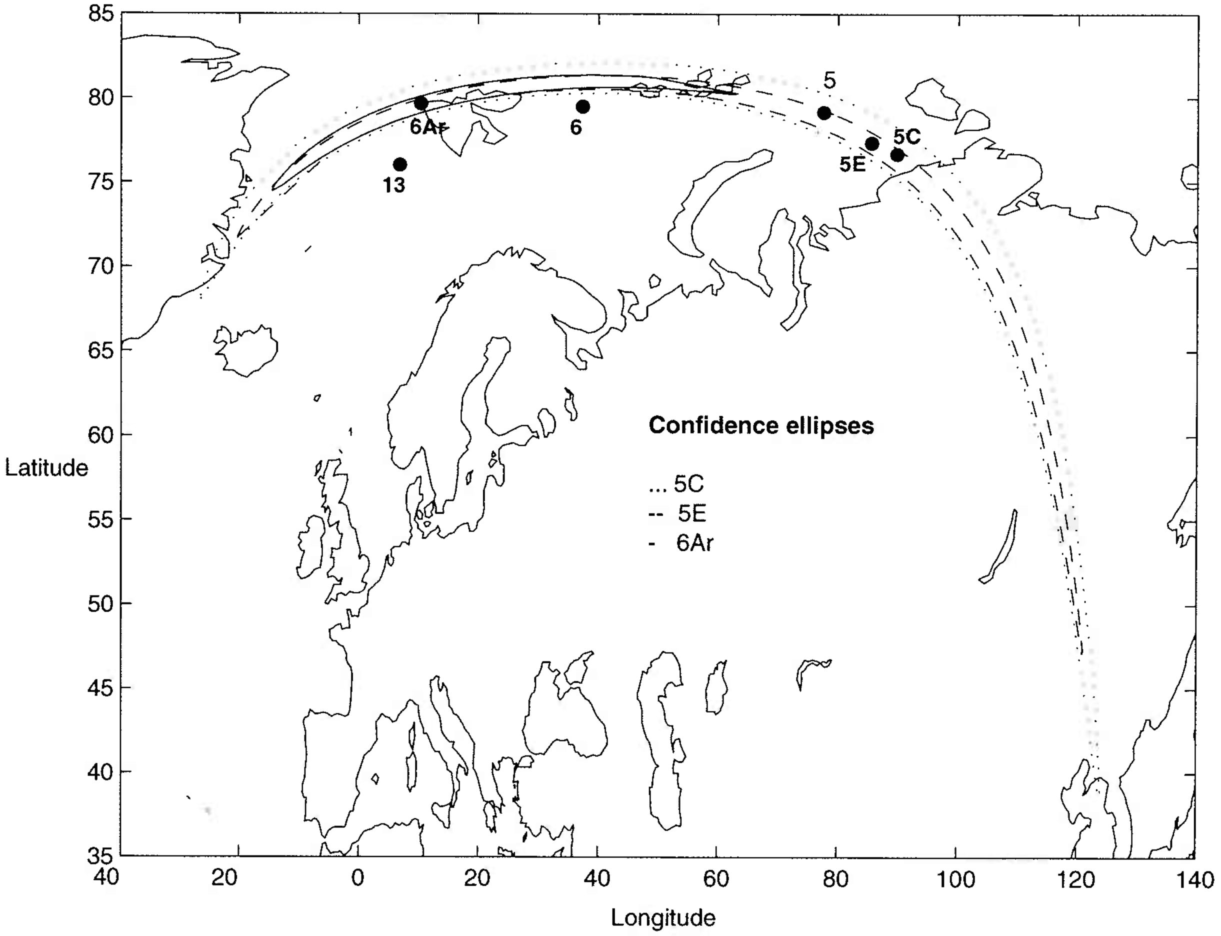

Figure 9: Plot of derived reconstruction poles (anomalies 6Ar, 5E, 5C) using the Hellinger-Chang method, with their 95% confidence ellipses; the Klitgord-Schouten poles (anomalies 13, 6, 5) are also shown.

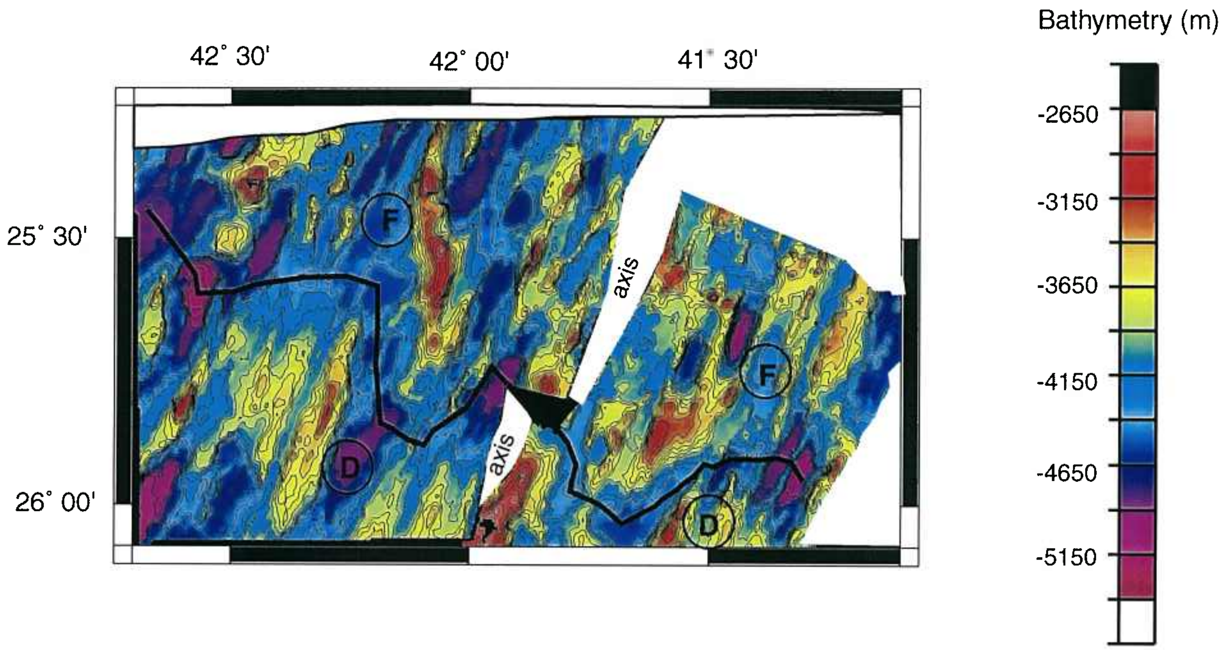

Figure 10: Map of Mid-Atlantic Ridge east- and west-flank bathymetry reconstructed to the time of anomaly 6Ar (22.62 Ma), ~0.3 m.y. before the initial breakaway that formed a megamullion complex in the southern portion of segment F. The contour interval is 100m. The African plate (east flank) is fixed. Areas of overlap at the ridge axis are shown in black and areas of underlap are shown in white (the northeast, southeast, and northwest corners are areas of no data). The right-lateral-offset discontinuity between segments D and F is delineated in black. Segment F will divide into segments G and H, and the southern of these two segments (segment G) will subsequently develop the megamullion complex (see Figure 13).

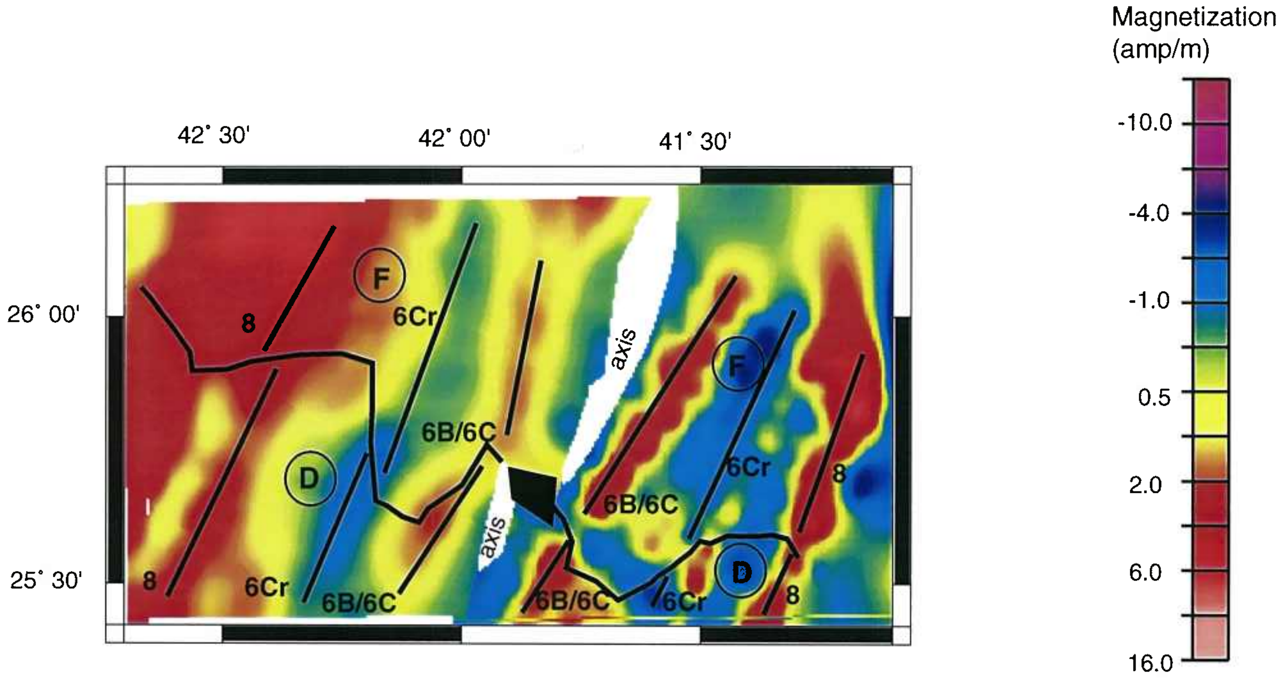

Figure 11: Map of Mid-Atlantic Ridge east- and west-flank crustal magnetization reconstructed to the time of anomaly 6Ar (22.62 Ma), ~0.3 m.y. before the initial breakaway that formed a megamullion complex in the southern portion of segment F. African plate (east flank) is fixed. Areas of overlap at the ridge axis are shown in black and areas of underlap are shown in white. The right-lateral-offset discontinuity between segments D and F is delineated in black. Chrons 6B/6C through 8 are identified and labeled. Different resolutions of anomalies on the east and west flanks is a result of different filtering when the data were inverted for magnetization (see text).

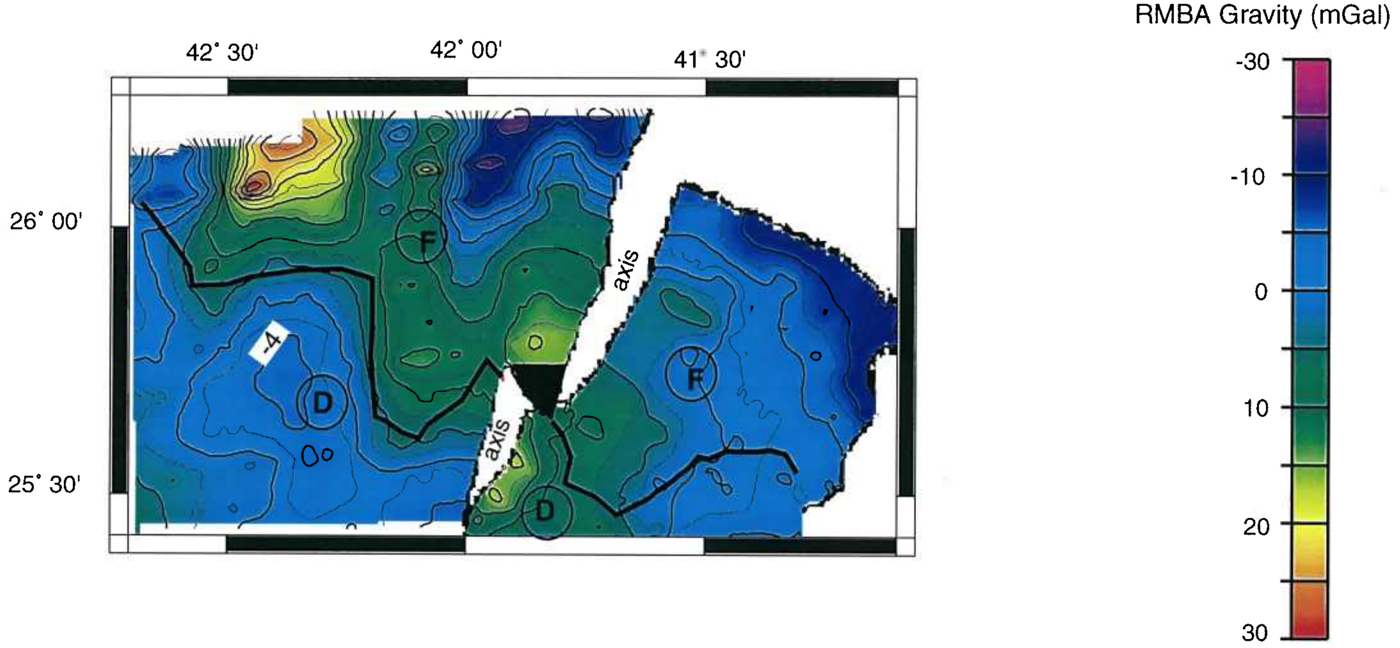

Figure 12: Map of Mid-Atlantic Ridge east- and west-flank gravity reconstructed to the time of anomaly 6Ar (22.62 Ma), ~0.3 m.y. before the initial breakaway that formed a megamullion complex in the southern portion of segment F. Values are RMBA deviations from the mean of the west-flank data plotted on the west flank, and deviations from the east-flank mean plotted on the east flank. Contour interval is 2 mGal. At the axis, areas of overlap are in black, and areas of underlap are in white. Note the elevated gravity values on the inside corner of segment D (southeast of the axial discontinuity) and the inside corner of segment F (northwest of the axial discontinuity).

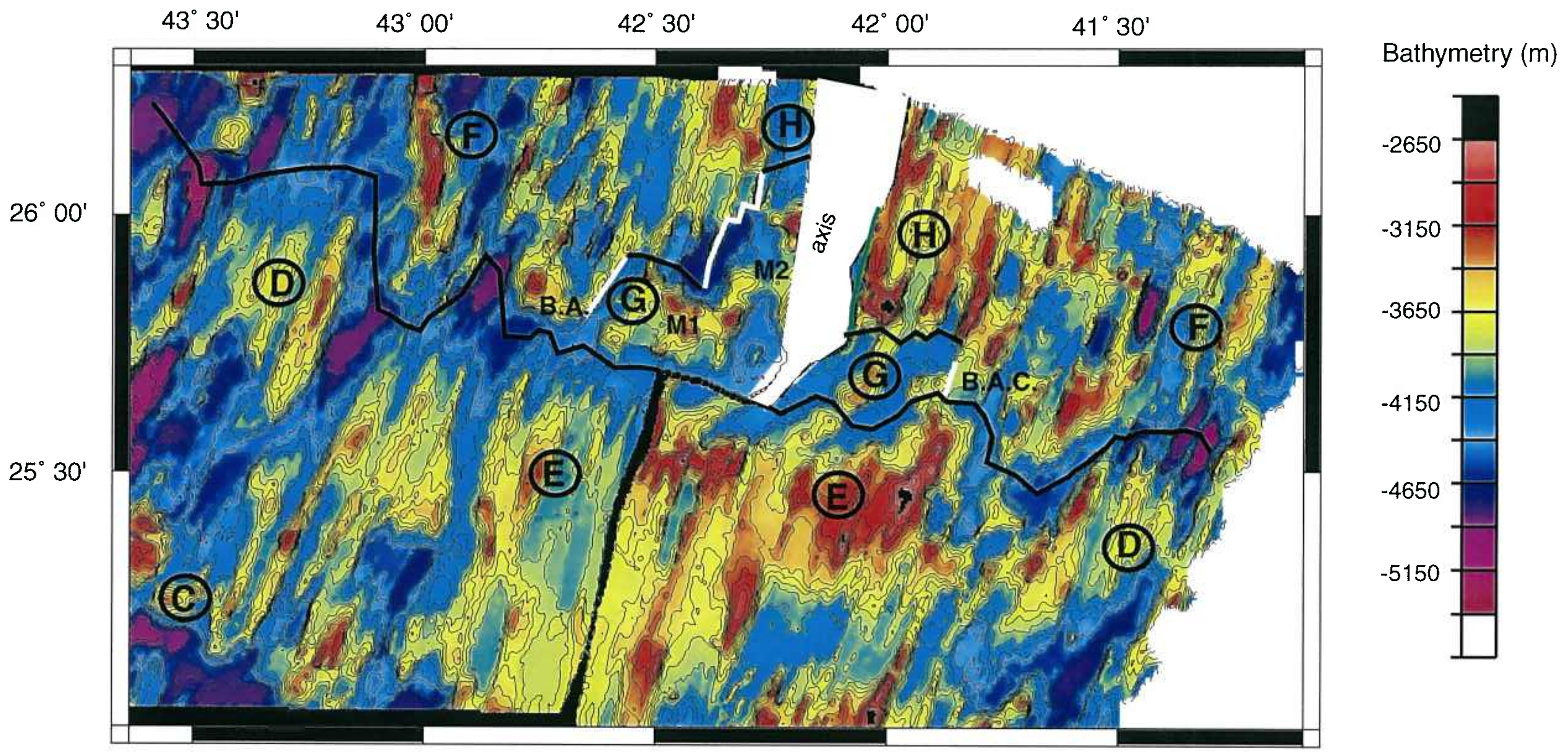

Figure 13: Map of Mid-Atlantic Ridge east- and west-flank bathymetry reconstructed to the time of anomaly 5E (19.88 Ma), ~2.4 m.y. after the onset of formation of the megamullion complex (M1, M2) in segment G. African plate (east flank) is fixed. Explanations as in Figure 10. Segment F has divided into segments G and H, and segments C and D have consolidated into segment E (Tucholke et al., 1997). The breakaways (B.A.) of megamullions M1 and M2 in the complex and the M1 breakaway conjugate (B.A.C.) are shown in white, and the M2 breakaway conjugate is shown in green.

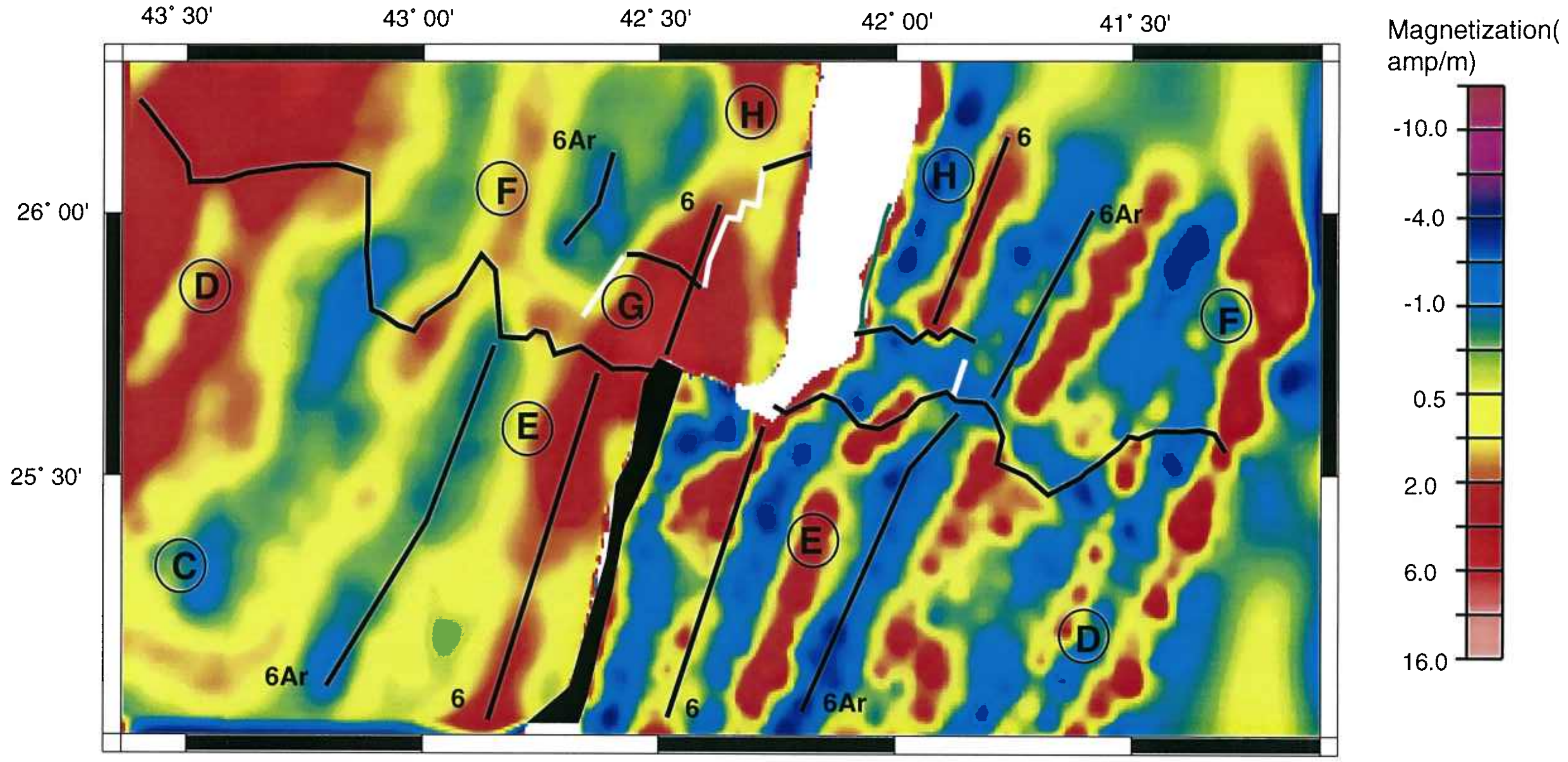

Figure 14: Map of Mid-Atlantic Ridge east- and west-flank crustal magnetization reconstructed to the time of anomaly 5E (19.88 Ma), ~2.4 m.y. after the onset of formation of the megamullion complex in segment G. Explanations as in Figures 11 and 13. Chrons 6 and 6Ar are labeled.

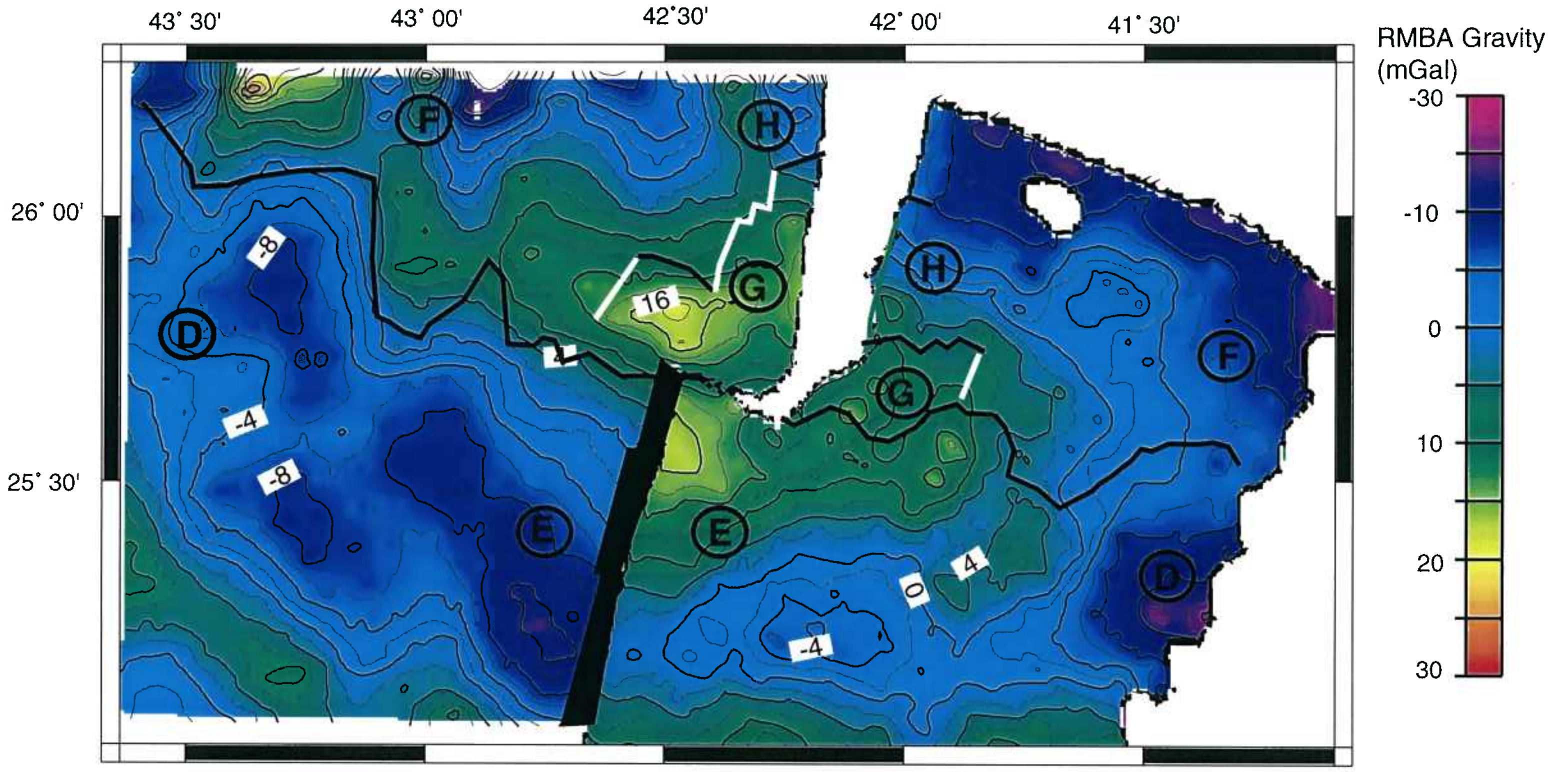

Figure 15: Map of Mid-Atlantic Ridge east- and west-flank gravity reconstructed to the time of anomaly 5E (19.88 Ma). Values are RMBA deviations from the mean of the west-flank data plotted on the west flank, and deviations from the east-flank mean plotted on the east flank. Explanations as in Figures 12 and 13.

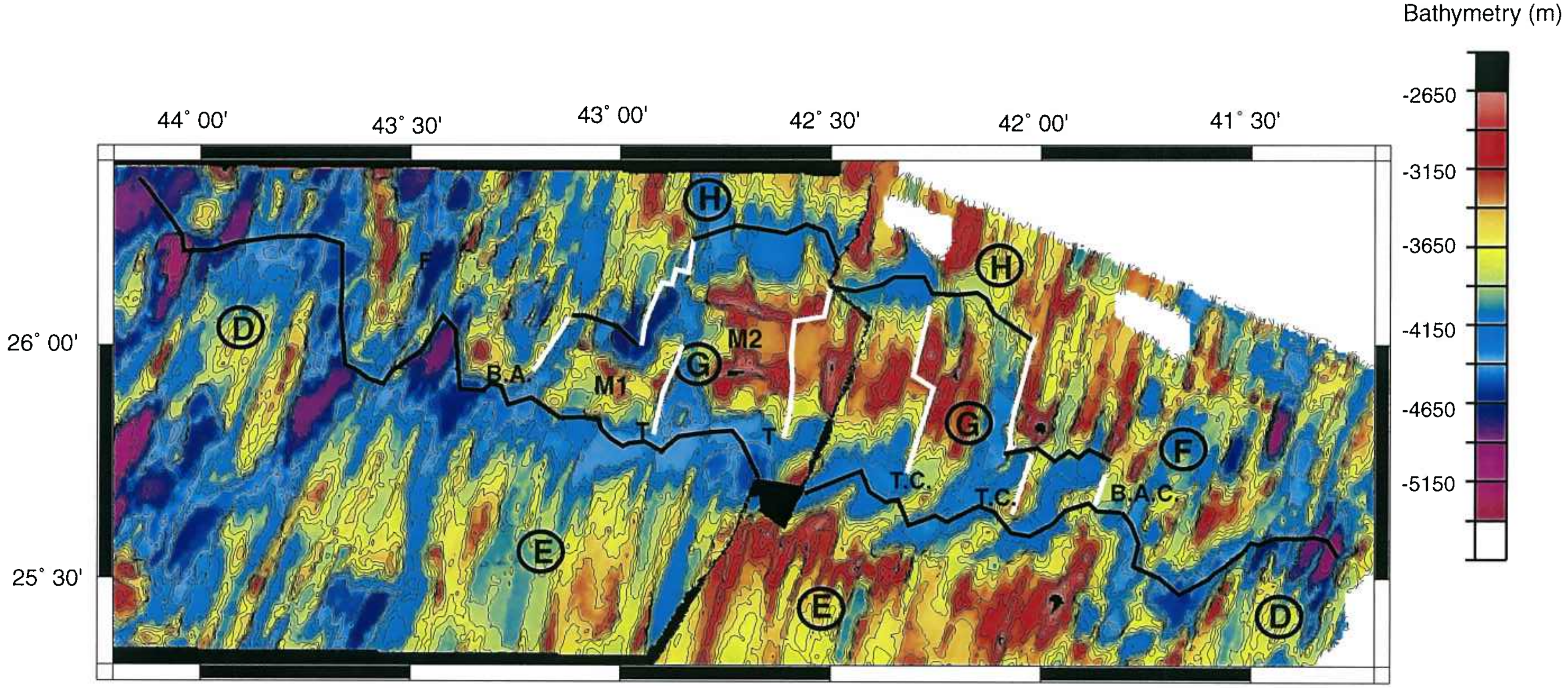

Figure 16: Map of Mid-Atlantic Ridge east- and west-flank bathymetry reconstructed to the time of anomaly 5C (17.58 Ma), ~1.0 m.y. after formation of the megamullion complex terminated in segment G. The African plate (east flank) is fixed. B.A. indicates the breakaway of megamullion M1 in the south and the subsequent breakaway of megamullion M2 in the north (both shown in white). B.A.C. indicates the breakaway conjugates, shown in white. T indicates the termination of megamullion M1 and M2, and T.C. is the termination conjugate. Areas of overlap along the ridge axis (~42°30'W) are in black. Areas of no data are white. Other explanations as in Figure 10.

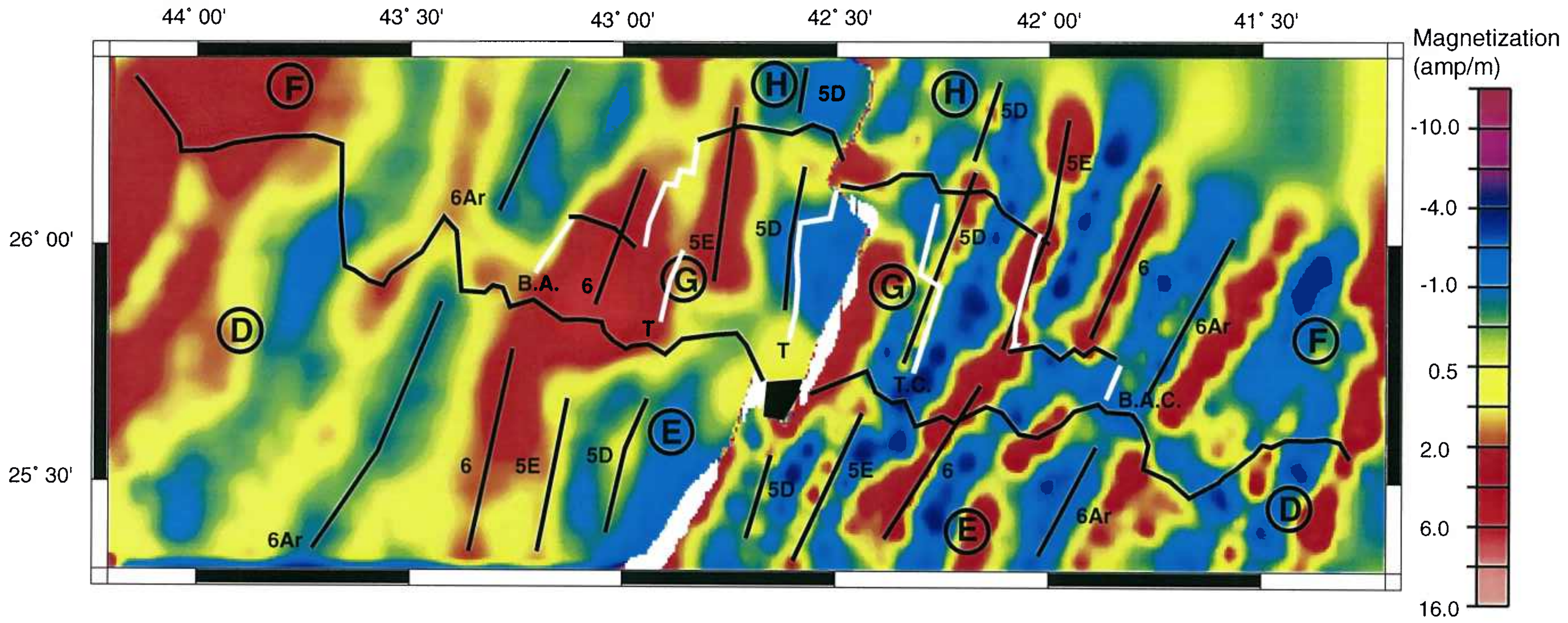

Figure 17: Map of Mid-Atlantic Ridge east- and west-flank crustal magnetization reconstructed to the time of anomaly 5C (17.58 Ma), ~1.0 m.y. after megamullion formation terminated in segment G. The African plate (east flank) is fixed. B.A. indicates the breakaway of megamullion M1 in the south and the subsequent breakaway of megamullion M2 in the north (both shown in white). B.A.C. indicates the breakaway conjugates, shown in white. T indicates the terminations of megamullion M1 and M2, and T.C. is the termination conjugate. Areas of overlap along the ridge axis (~42°30'W) are in black; areas of underlap are in white. Differences in underlap and overlap compared to Figures 16 and 18 occur because of different cell sizes in the gridded datasets. Chrons 5D through 8 are labeled.

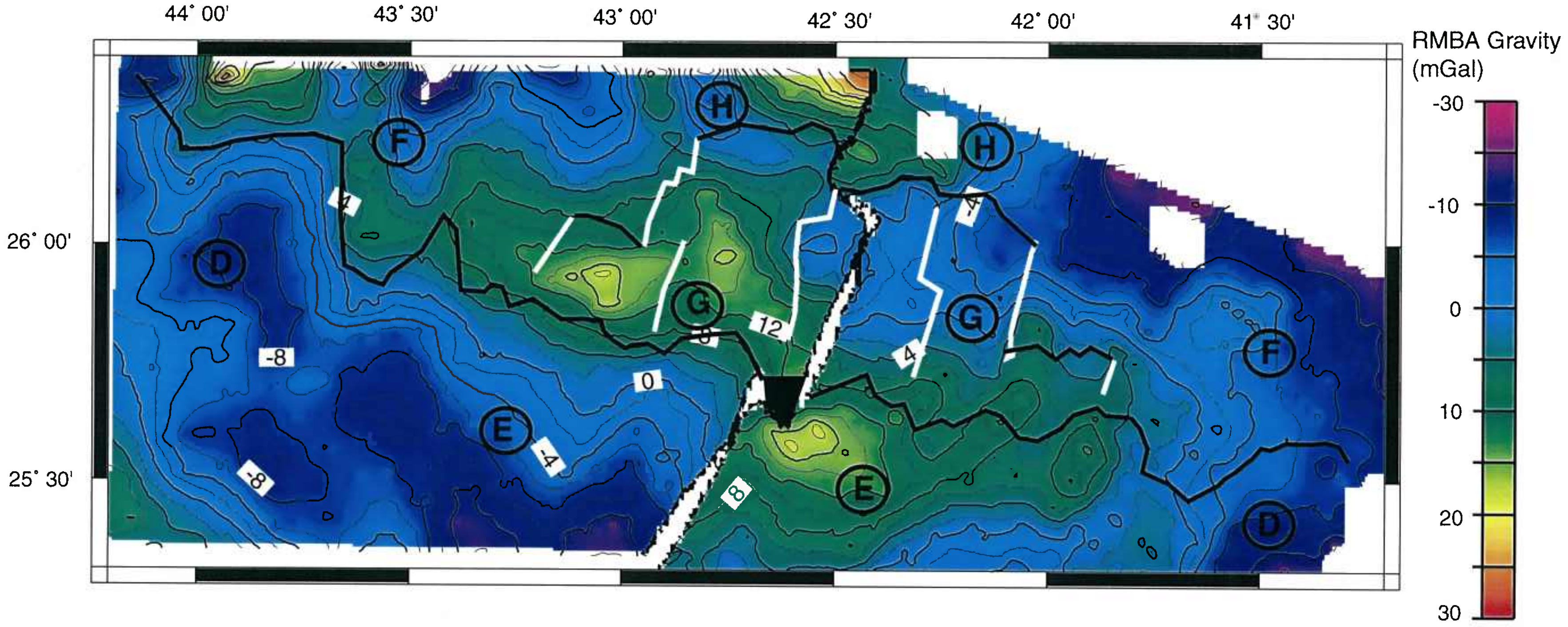

Figure 18: Map of Mid-Atlantic Ridge east- and west-flank gravity reconstructed to the time of anomaly 5C (17.58 Ma), ~1.0 m.y. after megamullion formation terminated in segment G. Values are RMBA deviations from the mean of the west-flank data plotted on the west flank, and deviations from the east-flank mean plotted on the east flank. Explanations as in Figures 12 and 16.

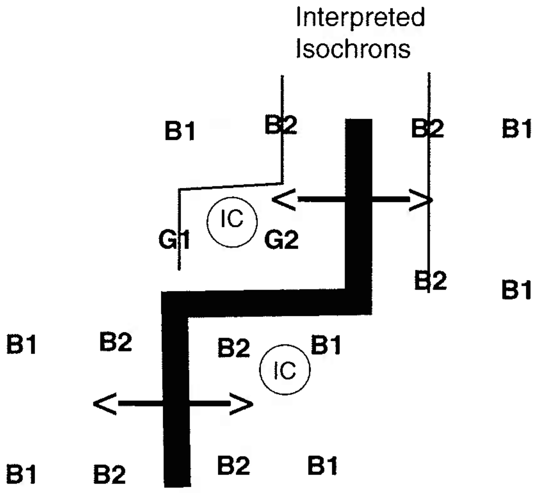

Figure 19: Plan-view diagram of a spreading-ridge axis offset by a right-lateral discontinuity, showing how a difference in the times when gabbro and basalt cooled below the Curie isotherm could increase the spacing of magnetic anomalies. IC indicates inside corners. The emplacement age of gabbro G1 and basalt B1 are the same, yet G1 would acquire its magnetic signature at the same time as B2 because it passes through the Curie isotherm at "B2 time". Either a lack of extrusive magmatism or exhumation of deep crust by faulting could account for the dominance of gabbroic crust, with a thin or missing basaltic layer, at inside corners.

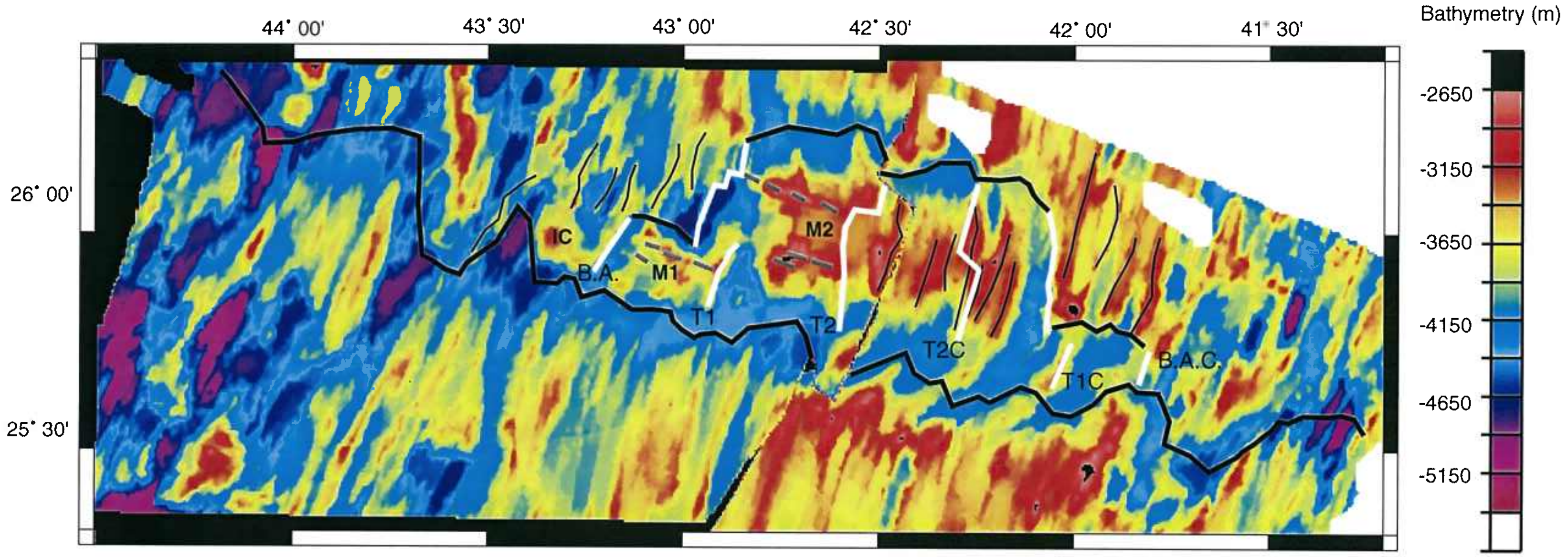

Figure 20: Reconstruction of bathymetry to the time of anomaly 5C with highly simplified structural interpretations. Black ridge-parallel lines are major axisward-dipping faults; prominent mullion structures are dashed in grey; B.A. is the breakaway of megamullion M1 in the south and megamullion M2 in the north (in white); T1 and T2 are the terminations of M1 and M2, respectively; B.A.C. is the breakaway conjugates (in white); T1C and T2C are the termination conjugates of M1 and M2, respectively.

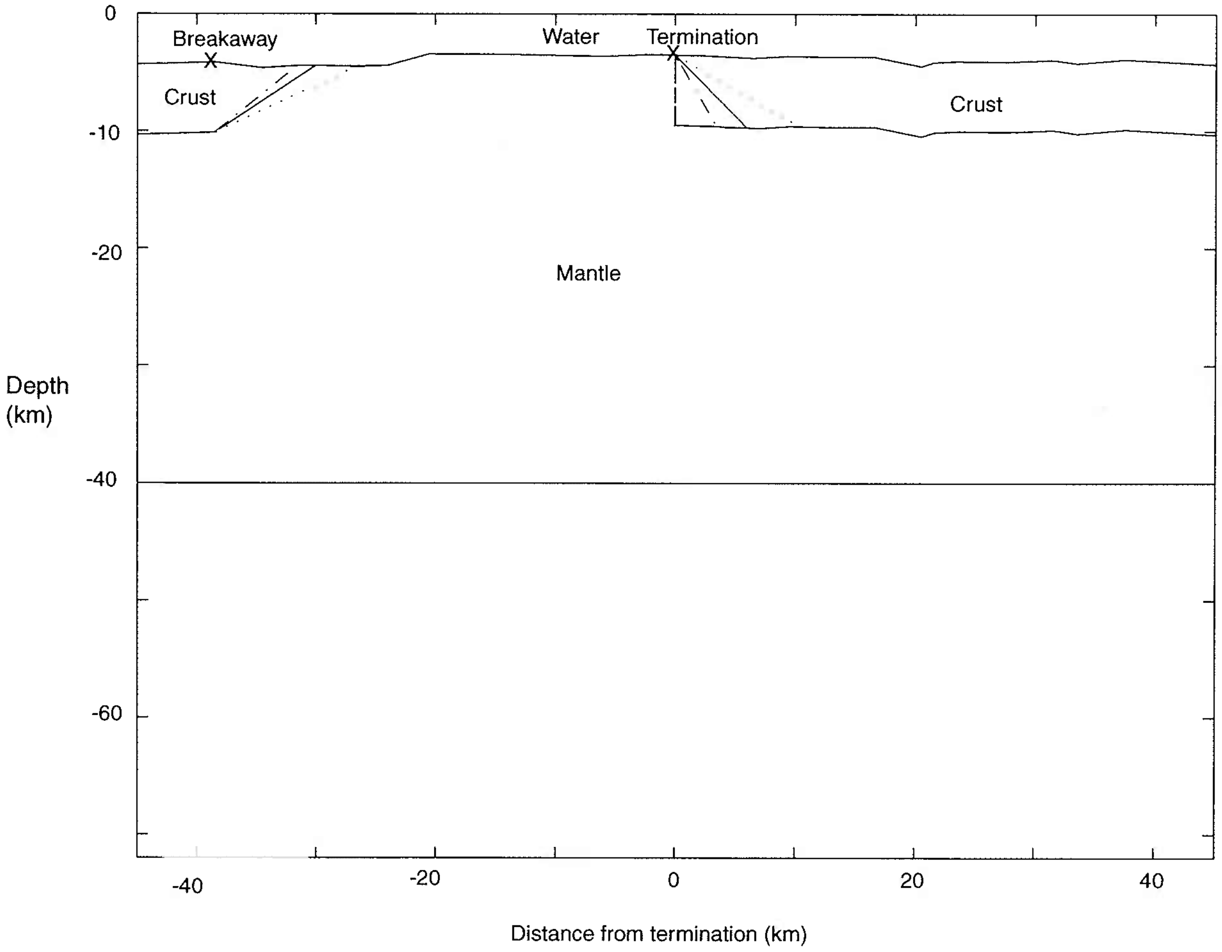

Figure 21: Idealized structural cross section of a megamullion, showing four polygons used to model gravity (see text). The line at 40 km depth represents the depth extent of the model. The lines near the breakaway and termination show structure generated by four different dip angles of the detachment fault that formed the megamullion: dotted line represents a 30˚ fault; the solid line represents a 45˚ fault; the dash-dot line represents a 60˚ fault. The vertical dashed line at the termination is for an additional gravity model in which the western (breakaway) boundary is assumed to be 45˚.

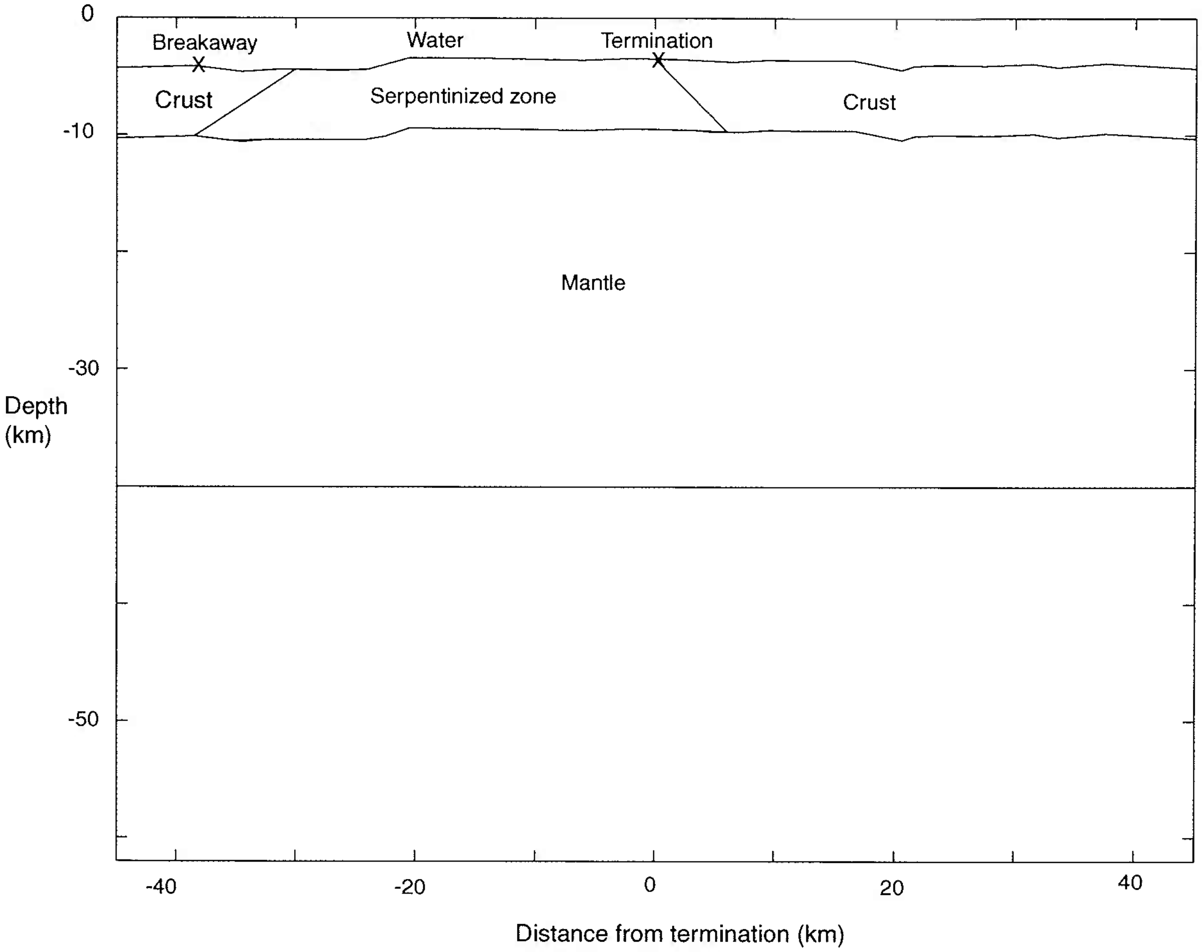

Figure 22: Idealized structural cross section of a megamullion, showing five polygons used to model gravity (see text). The line at 40 km depth is the extent of the model. The density in the serpentinized zone is varied to simulate 0%, 25%, 50%, 75%, and 100% serpentinization.

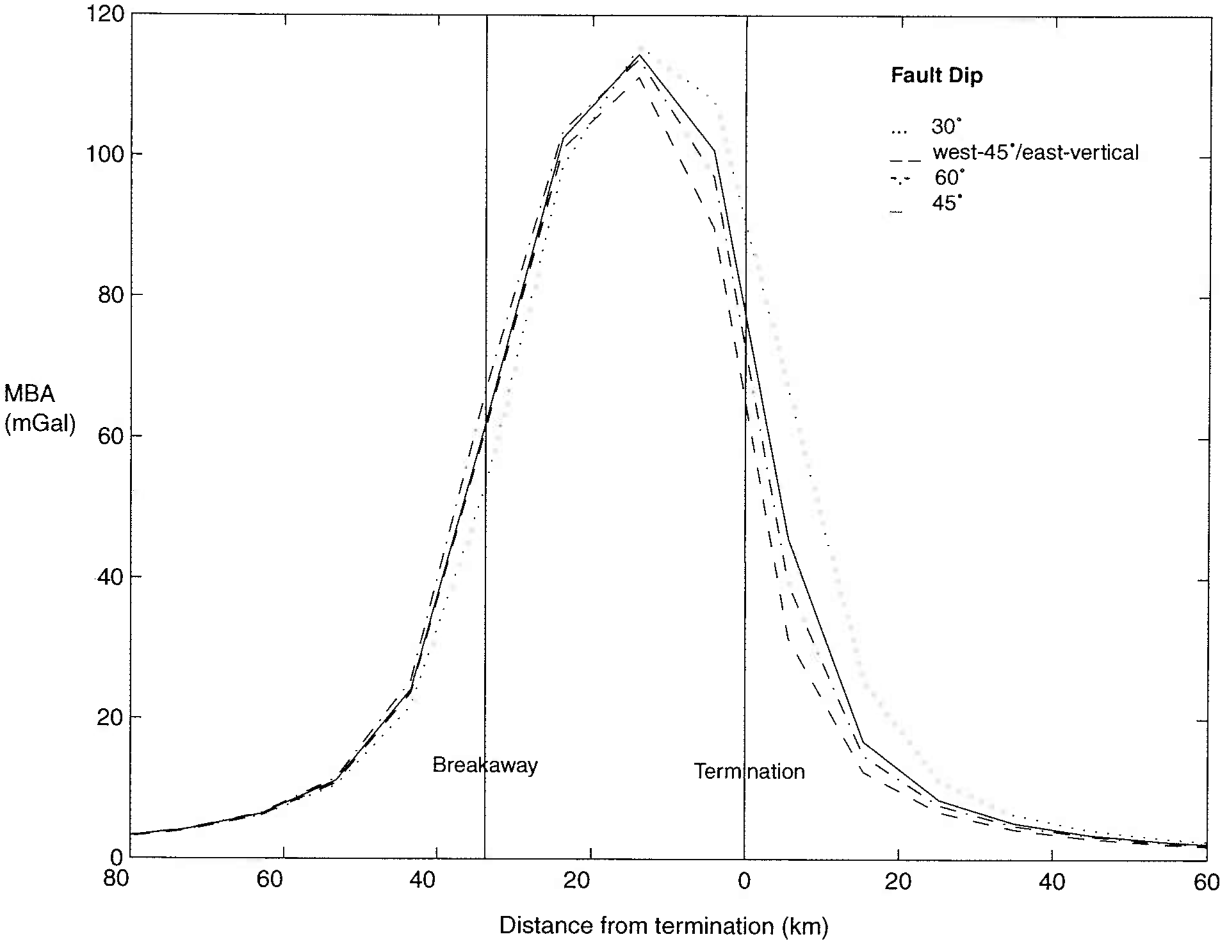

Figure 23: Predicted MBA gravity profiles for three different models of detachment fault dip,and one model with 45˚ dip at the breakaway and a vertical termination (see Figure 22). Gravity was calculated at nodes every 10 km, which causes the inflections observed in the profiles.

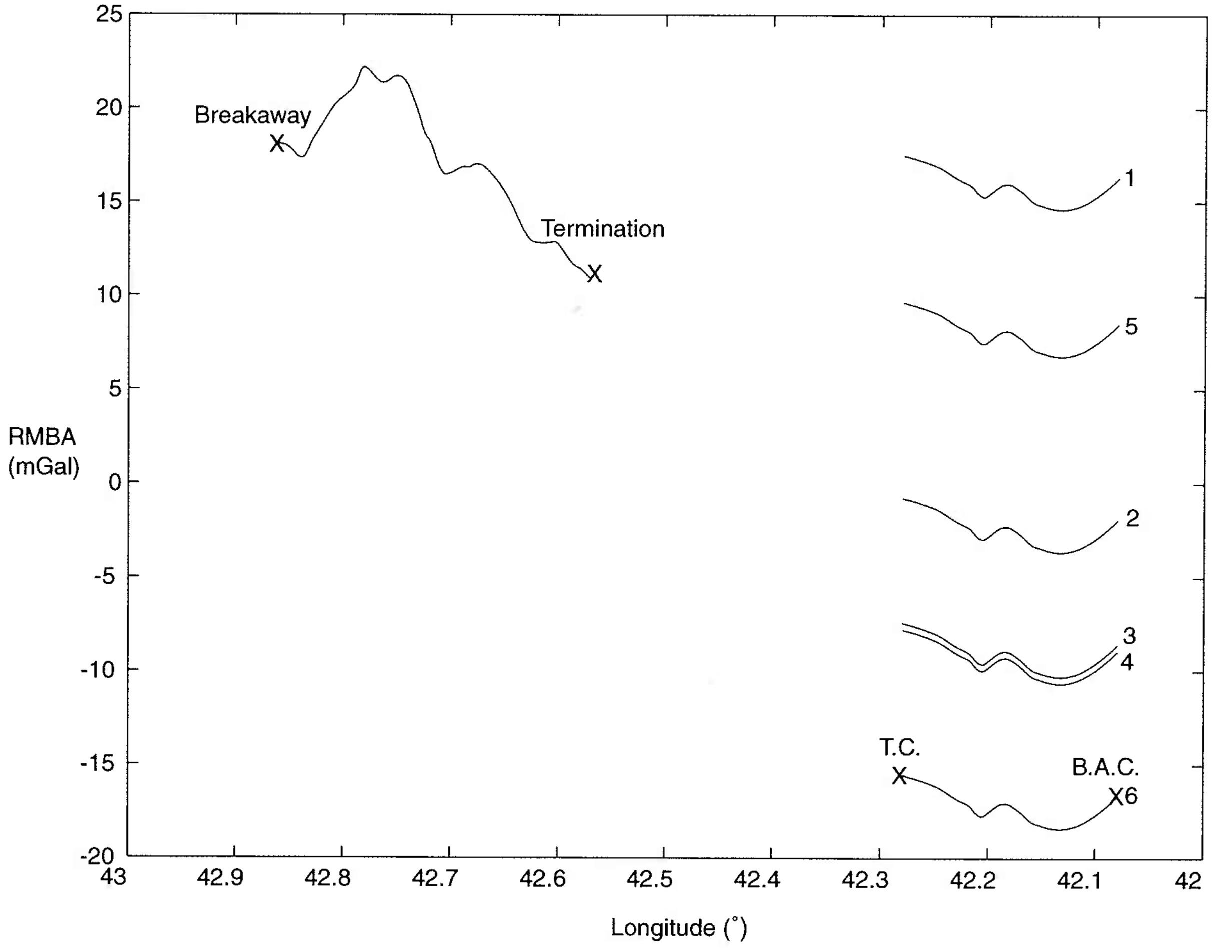

Figure 24: RMBA gravity along the northernmost profile of megamullion M2 (Profile A-A', Figure 29). T.C. and B.A.C. are the termination conjugate and breakaway conjugate, respectively. The west-flank profile and profile 6 (east flank) are the original RMBA data; profiles 1-4 are the adjusted data according to the corresponding calculated best fits of east-west Δg offsets (Figure 30). Profile 5 is adjusted to the average gravity difference between flanks at the location of the termination (see text).

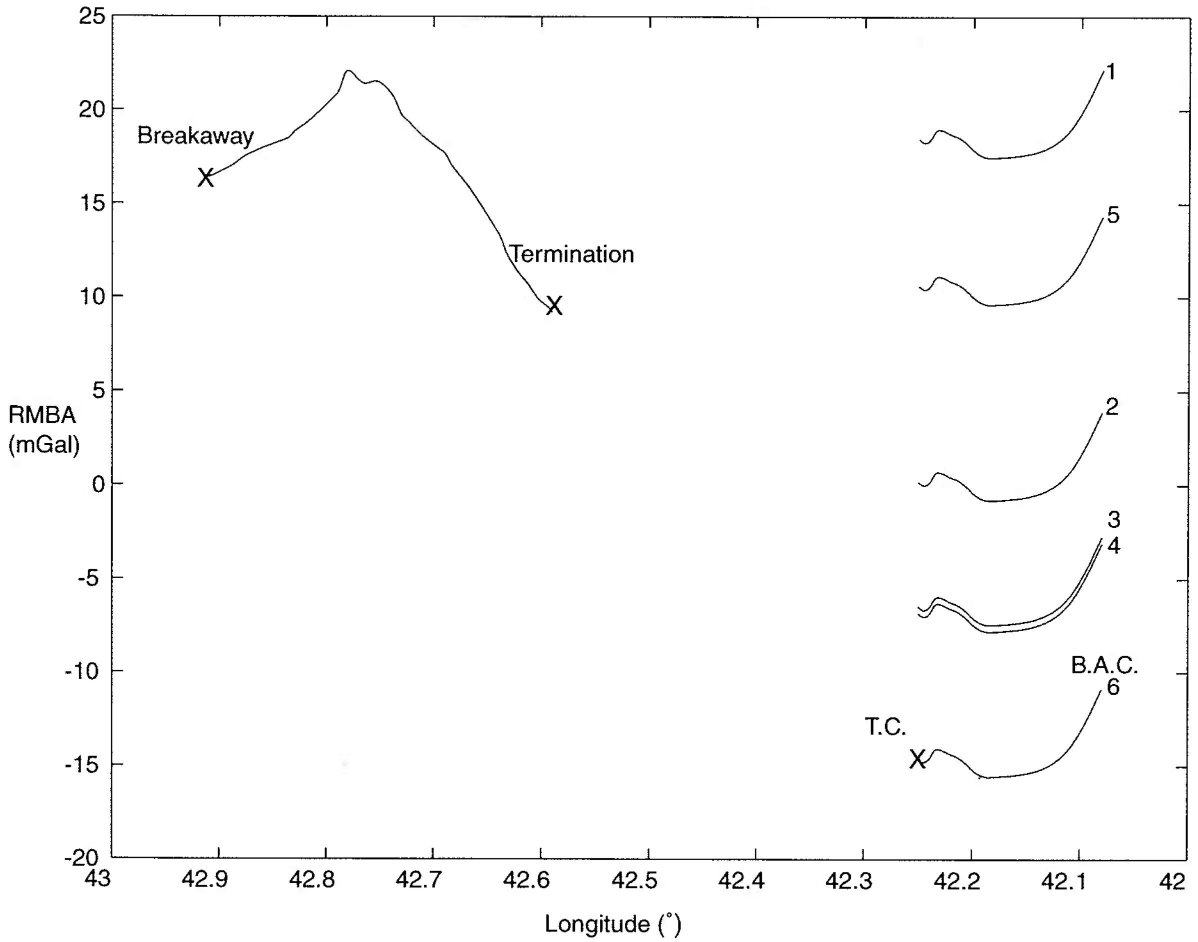

Figure 25: RMBA gravity along the central profile of megamullion M2 (Profile B-B', Figure 29). T.C. and B.A.C. are the termination conjugate and breakaway conjugate, respectively. The western flank profile and profile 6 (east flank) are the original RMBA data; profiles 1-4 are the adjusted data according to the corresponding calculated best fits of east-west Δ g offsets (Figure 30). Profile 5 is adjusted to the average gravity difference between flanks at the location of the termination (see text).

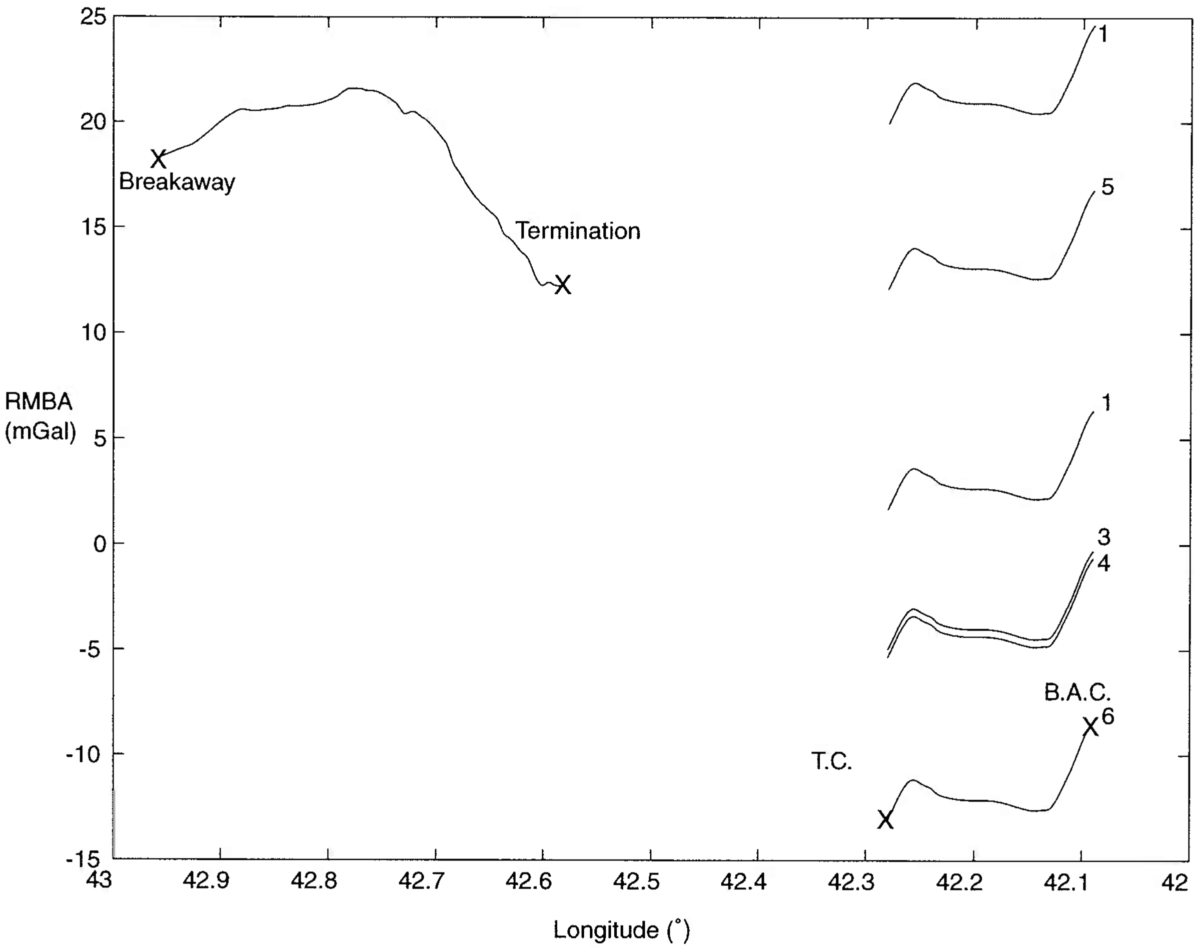

Figure 26: RMBA gravity along the southernmost profile of megamullion M2 (Profile C-C', Figure 29). T.C. and B.A.C. are the termination conjugate and breakaway conjugate, respectively. The west-flank profile and profile 6 (east flank) are the original RMBA data; profiles 1-4 are the adjusted data according to the corresponding calculated best fits of east-west Δ g offsets (Figure 30). Profile 5 is adjusted to the average gravity difference between flanks at the location of the termination (see text).

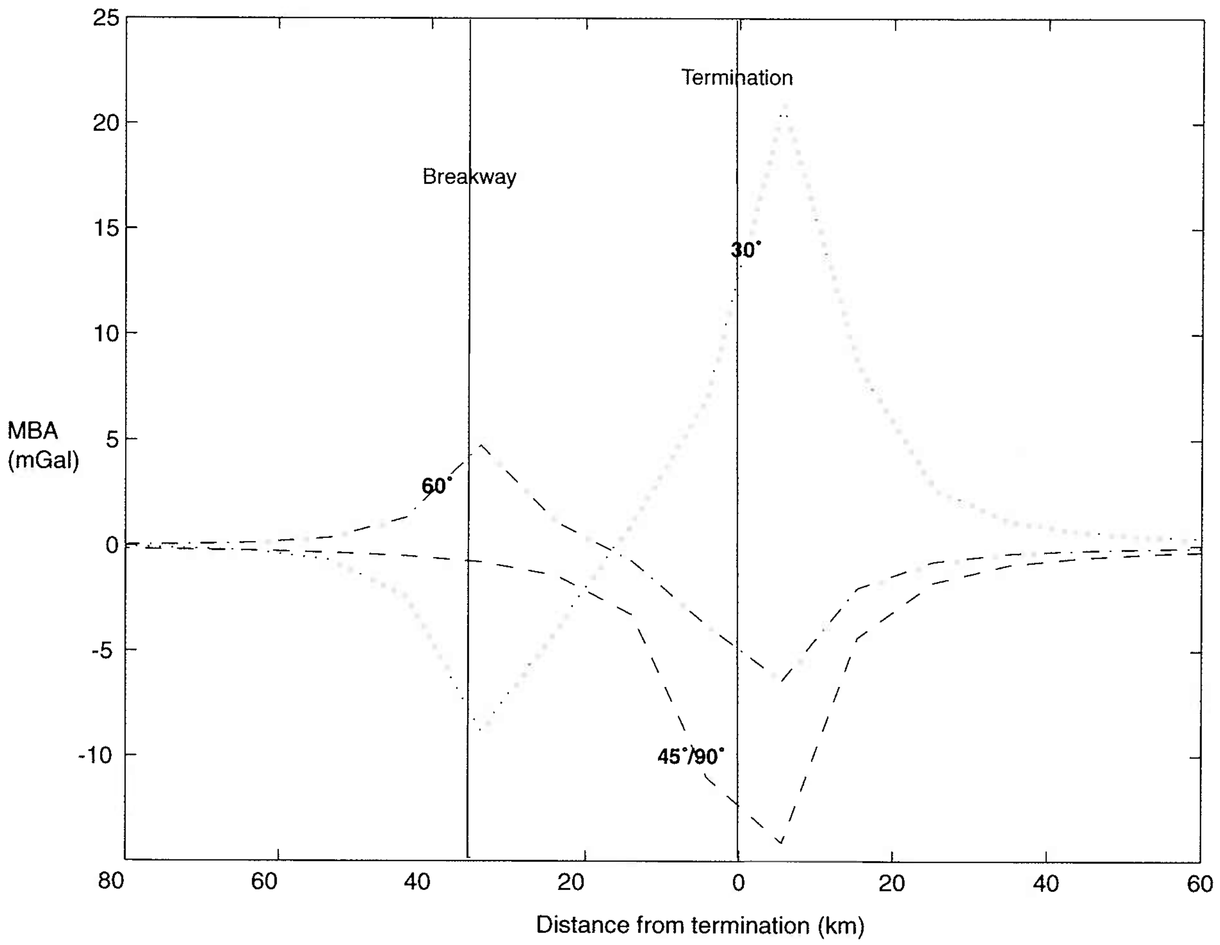

Figure 27: Difference of MBA gravity for 30˚, 60˚, 45˚/90˚ fault models compared to 45˚ fault model. Gravity was calculated at node spacing of 10 km.

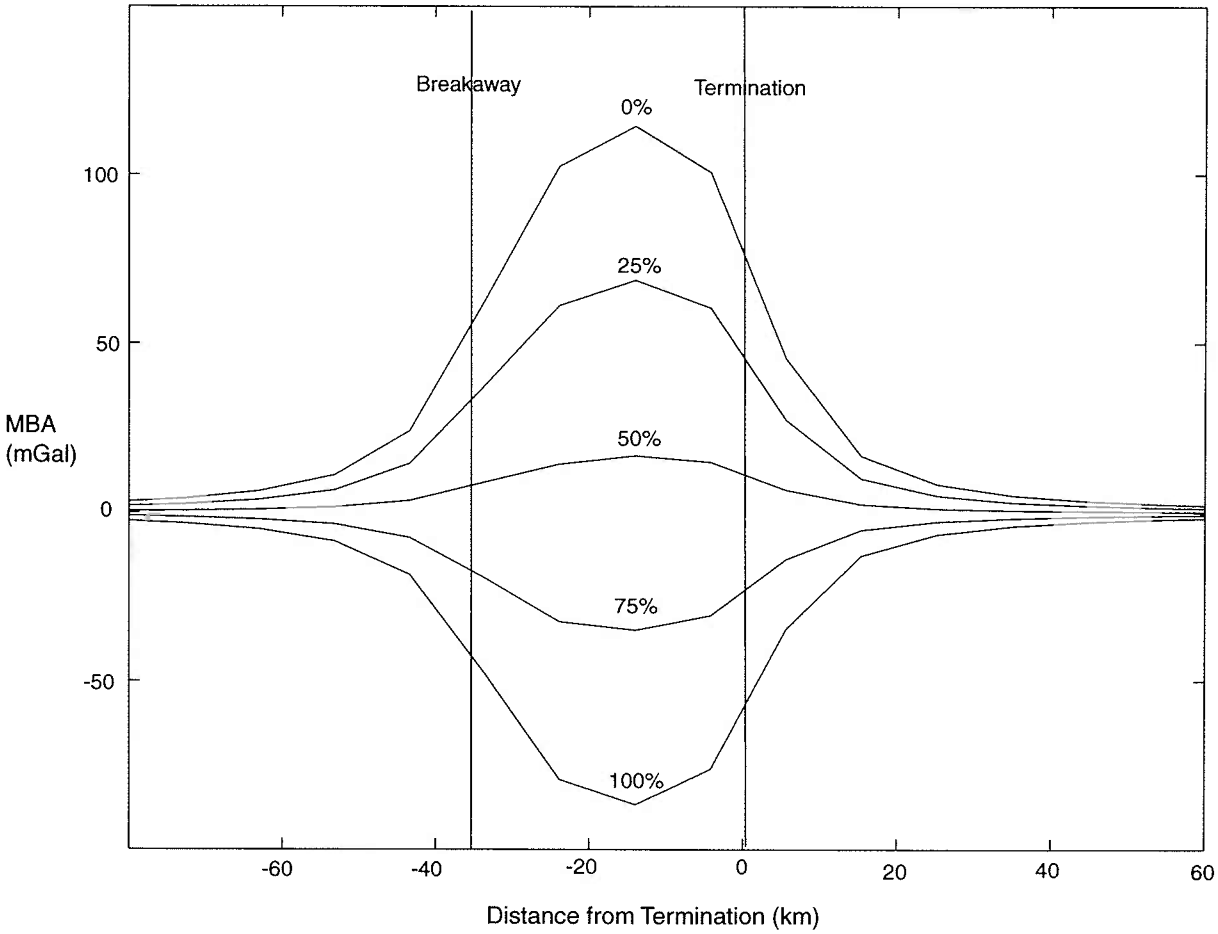

Figure 28: MBA gravity predicted from the five-polygon model for varying degrees of serpentinization of a 6-km-thick mantle wedge (Figure 22), assuming a 45° fault-dip model. Gravity was calculated at a node spacing of 10 km.

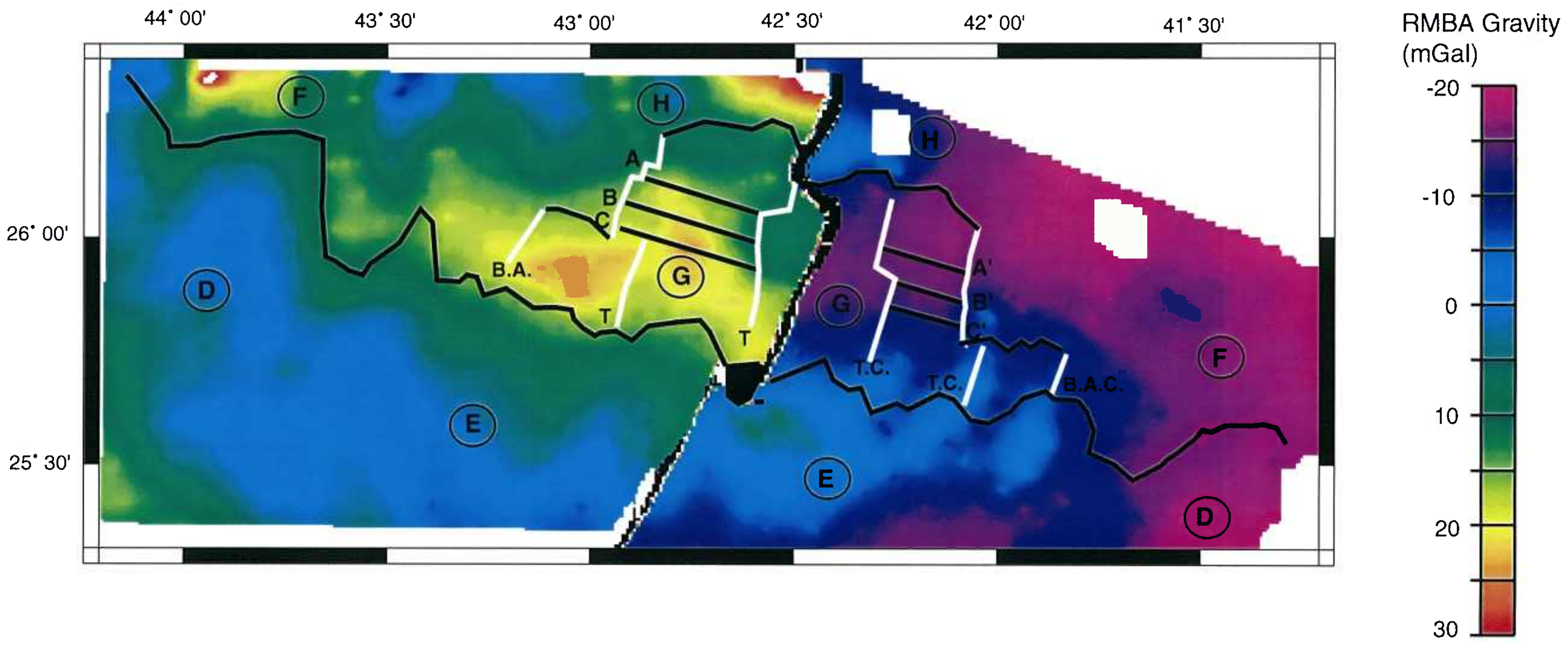

Figure 29: Plate reconstruction of observed RMBA gravity data to 17.58 Ma (anomaly 5C). Tracks A, B, and C are locations of gravity profiles across megamullion M2 and its conjugate, illustrated in Figures 24-26. Labels and explanations as in Figure 16.

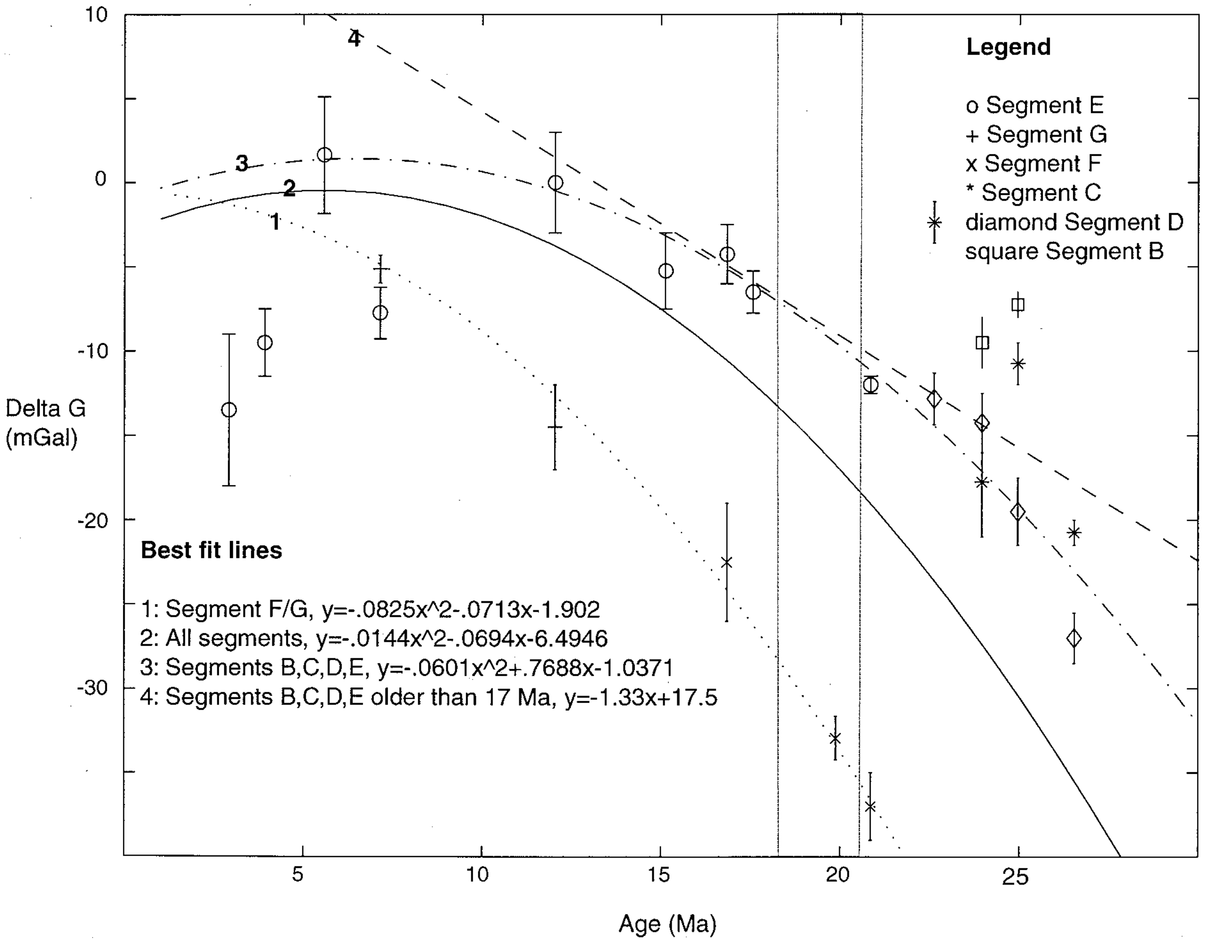

Figure 30: Plot of the difference in gravity values (east minus west) between east and west ridge flanks at segment centers, versus age, with best-fit lines for segments and segment groups noted. Error bars are the variation in gravity at segment mid-points, within the range of uncertainty of mid-point location (see text). Box within vertical lines is the time span of formation of megamullion M2 (~20.6-18.3 Ma).